

**Using Carbon Dioxide to Enhance  
Recovery of Methane from Gas Hydrate  
Reservoirs: Final Summary Report**

B. P. McGrail  
H. T. Schaefer  
M. D. White  
T. Zhu  
A. S. Kulkarni  
R. B. Hunter  
S. L. Patil  
A. T. Owen  
P. F. Martin

September 2007

Prepared for  
the U.S. Department of Energy  
under Contract DE-AC06-76RLO 1830



## DISCLAIMER

This report was prepared as an account of work sponsored by an agency of the United States Government. Neither the United States Government nor any agency thereof, nor Battelle Memorial Institute, nor any of their employees, makes **any warranty, expressed or implied, or assumes any legal liability or responsibility for the accuracy, completeness, or usefulness of any information, apparatus, product, or process disclosed, or represents that its use would not infringe privately owned rights.** Reference herein to any specific commercial product, process, or service by trade name, trademark, manufacturer, or otherwise does not necessarily constitute or imply its endorsement, recommendation, or favoring by the United States Government or any agency thereof, or Battelle Memorial Institute. The views and opinions of authors expressed herein do not necessarily state or reflect those of the United States Government or any agency thereof.

PACIFIC NORTHWEST NATIONAL LABORATORY  
*Operated by*  
BATTELLE MEMORIAL INSTITUTE  
*for the*  
UNITED STATES DEPARTMENT OF ENERGY  
*under Contract DE-AC06-76RLO 1830*

**Printed in the United States of America**

**Available to DOE and DOE contractors from the  
Office of Scientific and Technical Information, P.O. Box 62, Oak Ridge,  
TN 37831;  
prices available from (615) 576-8401.**

**Available to the public from the National Technical Information Service,  
U.S. Department of Commerce, 5285 Port Royal Rd., Springfield, VA 22161**

**U.S. Department of Commerce, 5285 Port Royal Rd., Springfield, VA 22161**



This document was printed on recycled paper.

## **Executive Summary**

Although recent estimates (MILKOV et al., 2003) put the global accumulations of natural gas hydrate at 3,000 to 5,000 trillion cubic meters (TCM), compared against 440 TCM estimated (COLLETT, 2004) for conventional natural gas accumulations, how much gas could be produced from these vast natural gas hydrate deposits remains speculative. What is needed to convert these gas-hydrate accumulations to recoverable reserves are technological innovations, sparked through sustained scientific research and development. As with other unconventional energy resources, the challenge is to first understand the resource, its coupled thermodynamic and transport properties, and then address production challenges.

Carbon dioxide sequestration coupled with hydrocarbon resource recovery is often economically attractive. Use of CO<sub>2</sub> for enhanced recovery of oil, conventional natural gas, and coal-bed methane are in various stages of common practice. In this report, we discuss a new technique utilizing CO<sub>2</sub> for enhanced recovery of natural gas hydrate. We have focused our attention on the Alaska North Slope where approximately 640 Tcf of natural gas reserves in the form of gas hydrate have been identified. Alaska is also unique in that potential future CO<sub>2</sub> sources are nearby, and petroleum infrastructure exists or is being planned that could bring the produced gas to market or for use locally.

The EGHR (Enhanced Gas Hydrate Recovery) concept discussed in this report takes advantage of the physical and thermodynamic properties of mixtures in the H<sub>2</sub>O-CO<sub>2</sub> system combined with controlled multiphase flow, heat, and mass transport processes in hydrate-bearing porous media. A chemical-free method is used to deliver a L<sub>CO<sub>2</sub></sub>-L<sub>w</sub> microemulsion into the gas hydrate bearing porous medium. The microemulsion is injected at a temperature higher than the stability point of methane hydrate, which upon contacting the methane hydrate decomposes its crystalline lattice and releases the enclathrated gas. Conversion of the microemulsion to CO<sub>2</sub> hydrate occurs over time as controlled by heat transfer, diffusion, and the intrinsic kinetics of CO<sub>2</sub> hydrate formation. Sensible heat of the emulsion and heat of formation of the CO<sub>2</sub> hydrate provide a low grade heat source for further dissociation of methane hydrate away from the injectate plume. Process control is afforded by variation in the temperature of the emulsion, ratio of CO<sub>2</sub> and water, and droplet size of the discrete CO<sub>2</sub> phase. Small scale column experiments show injection of the emulsion into a methane hydrate rich sand results in the release of CH<sub>4</sub> gas and the formation of CO<sub>2</sub> hydrate. The experimental results were verified with computer modeling using the STOMP-HYD simulator, which showed over 3X enhancement in production rate using the EGHR technique when compared with warm water injection alone.

The gas exchange technology (including EHGR) releases methane by replacing it with a more thermodynamic molecule (e.g., carbon dioxide). This technology has four advantageous: 1) it sequesters a greenhouse gas (CO<sub>2</sub>), 2) it releases energy via an exothermic reaction, and 3) it retains the mechanical stability of the hydrate reservoir, and 4) produced water can be used to form the emulsion and recycled into the reservoir thus eliminating a disposal problem in arctic settings.

Page intentionally left blank

# CONTENTS

1.0	Introduction.....	1
1.1	Gas Hydrate Occurrence.....	1
1.2	Production of methane from Gas Hydrate Reservoirs.....	1
1.2.1	Thermal Stimulation.....	2
1.2.2	Depressurization.....	2
1.2.3	Inhibitor Injection.....	3
1.2.4	Gas Exchange.....	3
2.0	Experimental.....	7
2.1	Gas Phase Exchange Experiments.....	7
2.2	Single-Phase Injection Experiments.....	8
2.3	L <sub>CO2</sub> -L <sub>w</sub> Emulsion Injection Experiments.....	9
2.4	Continuous Microemulsion Injection Experiments.....	12
2.4.1	Microemulsion injector.....	12
2.4.2	Microemulsion Injection Experiments.....	13
3.0	Modeling.....	19
3.1	Mathematical Model.....	19
3.1.1	Governing Equations.....	19
3.1.2	Phase Saturations.....	20
3.2	Numerical Solution.....	21
3.2.1	Discretization and Linearization.....	21
3.2.2	Primary Variable Switching.....	22
3.3	Application.....	23
3.3.1	Pure Water Injection.....	25
3.3.2	Liquid-CO <sub>2</sub> Microemulsion Injectant.....	26
4.0	Discussion.....	29
5.0	Conclusion.....	31
6.0	References.....	33



## FIGURES

1.	Distribution of gas hydrates on the North Slope of Alaska (MORIDIS et al., 2004).....	1
2.	Carbon dioxide exchange in bulk CH <sub>4</sub> hydrate as function of time at three different temperatures (0°, 2.5°, and 4°C).....	7
3.	Schematic showing injection path of CO <sub>2</sub> saturated water into a sand packed HYDEX® 301 column.....	8
4.	Temperature profile as a function of time after injection of CO <sub>2</sub> saturated water into a sand packed HYDEX® 301 column .....	9
5.	Density of liquid water and CO <sub>2</sub> as a Function of Pressure at 15°C.....	9
6.	Schematic showing injection path of L <sub>CO2</sub> -L <sub>w</sub> into a CH <sub>4</sub> rich hydrate sand packed HYDEX® 301 column.....	10
7.	View through quartz window into magnetically stirred pressure cell containing liquid CO <sub>2</sub> and water at 15°C and 1000 psig .....	10
8.	Temperature of sand packed column as a function of time, following injection of L <sub>CO2</sub> -L <sub>w</sub> emulsion .....	11
9.	Schematic of microemulsion injector .....	12
10.	High speed photograph (500 fps) of L <sub>CO2</sub> -L <sub>w</sub> microemulsion created inside a sapphire high pressure column (2.54 cm OD). .....	13
11.	Schematic showing the high pressure sapphire cell equipped with a multi-port thermocouple probe .....	14
12.	Schematic showing the redesigned high pressure sapphire cell equipped with a bypass port and cooling shroud.....	14
13.	Raman spectra of CH <sub>4</sub> as vapor, aqueous dissolved, and gas hydrate (porous media).....	15
14.	Raman spectra of CO <sub>2</sub> as vapor, liquid, aqueous dissolved, and gas hydrate (porous media) .....	15
15.	Microemulsion injection valving schematic .....	16
16.	Temperature profile of HYDEX® 301 pressure cell during the formation of CH <sub>4</sub> hydrate, injection of CO <sub>2</sub> microemulsion, followed by the formation of CO <sub>2</sub> hydrate as a function of time .....	16
17.	Temperature profile of sapphire high pressure cell during the formation of CH <sub>4</sub> hydrate, injection of L <sub>CO2</sub> -L <sub>w</sub> microemulsion, followed by the formation of CO <sub>2</sub> hydrate as a function of time .....	17
18.	Gas analysis data collected during L <sub>CO2</sub> -L <sub>w</sub> microemulsion injection experiments .....	18
19.	CO <sub>2</sub> hydrate rich sand extracted from a column injected with L <sub>CO2</sub> -L <sub>w</sub> microemulsion. ....	18
20.	Hydrate saturation histories for 15°C pure-water injectant .....	25
21.	Hydrate saturation histories for 50°C pure-water injectant .....	26

22.	Hydrate saturation histories for 15°C, 50% volume liquid-CO <sub>2</sub> microemulsion injectant...	27
23.	Hydrate saturation histories for 25°C, 50% volume liquid-CO <sub>2</sub> microemulsion injectant...	27
24.	ANS well log temperature data shown as shaded area (after Collett 1993). .....	29
25.	Schematic of down borehole injection tool.....	30

**TABLES**

3.1.	Conceptual Phase Conditions and Primary Variable Sets .....	22
3.2.	Implemented Phase Conditions and Primary Variable Sets.....	23
3.3.	Hydrologic Parameters and Initial Conditions.....	24
3.4.	Hydrate Production Scenarios.....	24
3.5.	Liquid-CO <sub>2</sub> Microemulsion Injectant Simulation Results .....	26

## NOMENCLATURE

- $\mathbf{D}_{h_\gamma}$  phase hydraulic dispersion coefficient,  $\text{m}^2/\text{s}$
- $D_\gamma^i$  diffusion coefficient of component  $i$  in phase  $\gamma$ ,  $\text{m}^2/\text{s}$
- $g$  acceleration of gravity,  $\text{m}/\text{s}^2$
- $h_g^i, h_\gamma$  gas of component  $i$ , phase enthalpy,  $\text{J}/\text{kg}$
- $\mathbf{J}_\gamma^i$  diffusive flux of component  $i$  in phase  $\gamma$ ,  $\text{kg}/\text{m}^2 \text{ s}$
- $\mathbf{k}$  intrinsic permeability,  $\text{m}^2$
- $\mathbf{k}_e$  equivalent thermal conductivity,  $\text{W}/\text{m K}$
- $k_{r\gamma}$  phase relative permeability
- $L_w$  liquid water
- $L_{\text{CO}_2}$  liquid  $\text{CO}_2$
- $\dot{m}_\gamma$  phase mass source rate,  $\text{kg}/\text{s}$
- $M^i, M_\gamma$  component, phase molecular weight,  $\text{kg}/\text{kmol}$
- $P_g, P_h, P_i, P_l, P_n, P_\gamma$  gas, hydrate, ice, aqueous, liquid- $\text{CO}_2$ , phase pressure, Pa
- $P_g^a, P_g^o, P_g^w$   $\text{CO}_2, \text{CH}_4, \text{H}_2\text{O}$  vapor partial pressure
- $P_{nc}$  liquid- $\text{CO}_2$  critical pressure
- $P_{sat}^a$  saturated  $\text{CO}_2$  vapor pressure
- $\dot{q}$  energy source rate, W
- $r_{hl}, r_{il}$  hydrate-aqueous, ice-aqueous radius, m
- $s_g, s_h, s_i, s_l, s_n, s_t$  gas, hydrate, ice, aqueous, liquid- $\text{CO}_2$ , total-liquid saturation
- $\bar{s}_g, \bar{s}_h, \bar{s}_i, \bar{s}_l, \bar{s}_n, \bar{s}_t$  effective gas, hydrate, ice, aqueous, liquid- $\text{CO}_2$ , total-liquid saturation
- $\bar{s}_{hl}, \bar{s}_{il}$  effective hydrate-aqueous, ice-aqueous saturation
- $\bar{\bar{s}}_l, \bar{\bar{s}}_t$  apparent aqueous, total-liquid saturation
- $s_{lr}$  residual aqueous saturation
- $s_\gamma$  phase saturation
- $t$  time, s
- $T$  temperature, K
- $T_{eq}^{ex}, T_{fp}^{ex}$  ex-situ hydrate equilibrium, ice freezing point temperature, K
- $u_l, u_s, u_\gamma$  aqueous, precipitated salt, phase internal energy,  $\text{J}/\text{kg}$
- $\mathbf{V}_\gamma$  phase volumetric flux,  $\text{m}/\text{s}$
- $\mathbf{z}_g$  gravitational unit vector
- $\beta_{gl}, \beta_{gn}$  gas-aqueous, gas-liquid  $\text{CO}_2$  scaling factor
- $\beta_{hl}, \beta_{il}, \beta_{nl}$  hydrate-aqueous, ice-aqueous, liquid  $\text{CO}_2$ -aqueous scaling factor
- $\theta_{gn}, \theta_{nl}$  gas-liquid  $\text{CO}_2$ , liquid  $\text{CO}_2$ -aqueous contact angle, radian

$\mu_\gamma$  phase viscosity, Pa s

$\zeta_l^s$  total salt aqueous mass fraction

$\rho_l, \rho_s, \rho_\gamma$  aqueous, precipitated-salt, phase density, kg/m<sup>3</sup>

$\sigma^{ref}$  reference interfacial tension, dynes/cm

$\sigma_{gl}, \sigma_{gn}$  gas-aqueous, gas-liquid CO<sub>2</sub> interfacial tension, dynes/cm

$\sigma_{hl}, \sigma_{il}, \sigma_{nl}$  hydrate-aqu., ice-aqueous, liquid CO<sub>2</sub>-aqueous interfacial tension, dynes/cm

$\tau_\gamma$  phase tortuosity factor

$\phi_D, \phi_T$  diffusive, total porosity

$\chi_\gamma^i$  mole fraction of component  $i$  in phase  $\gamma$

$\psi$  entry pressure, Pa

$\omega_\gamma^i$  mass fraction of component  $i$  in phase  $\gamma$

## 1.0 INTRODUCTION

### 1.1 GAS HYDRATE OCCURRENCE

Clathrate hydrates are solid crystalline “inclusion” compounds, which form when water (the host) is contacted with small hydrophobic molecules (the guest) such as methane, ethane, H<sub>2</sub>S, and CO<sub>2</sub> (ENGLEZOS, 1993; SLOAN, 1998) under certain pressure and temperature conditions. When the guest molecule is a constituent of natural gas, clathrate hydrates are also referred to as gas hydrates (SLOAN, 1998). Solid gas hydrates occur generally in two types of geologic settings: 1) on land in permafrost regions where cold temperatures persist in shallow sediments, and 2) beneath the ocean floor at water depths greater than about 500 meters where high pressures dominate (KVENVOLDEN et al., 1993). Although estimates of the amount of in situ hydrates vary considerably, even the most conservative estimate puts the amount of gas present as gas hydrates in the earth at 10<sup>15</sup> m<sup>3</sup> (KVENVOLDEN, 1995). This amount far exceeds all conventional energy reserves by as much as a factor of two and could provide for the energy demands of the planet well into the next century.

In 1995, the U.S. Geological Survey (USGS) conducted a study to assess the quantity of natural gas hydrate resources in the United States and found that the estimated quantity exceeded known conventional domestic gas resources (COLLETT, 2004). Recovery of natural gas from these hydrate-bearing deposits has the potential for being economically viable (COLLETT, 2004; MORIDIS et al., 2004; CIRCONI et al., 2005), but there remain significant technical challenges in converting these natural deposits into useable reserves (COLLETT, 2004).

The occurrence of gas hydrates on the Alaska North Slope was confirmed in 1972 in the northwest part of the PBU field (Collett; 1993, Thomas; 2001) and the North Slope now is known to contain several well-characterized gas hydrate deposits. The methane hydrate stability zone extends beneath most of the coastal plain province and has thicknesses >1000 m in the Prudhoe Bay area. Figure 1 depicts the distribution of the Eileen and Tarn gas hydrate accumulations in the area of the Prudhoe Bay, Kuparuk River, and Milne Point oil fields on the North Slope of Alaska. The estimated amount of gas within these gas hydrate accumulations is approximately 37 to 44 Tcf which is equivalent to twice the volume of conventional gas in the Prudhoe Bay field (Collett; 1993).

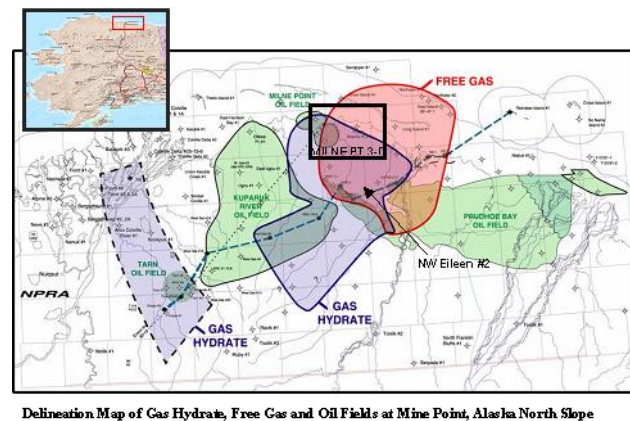


**Figure 1.** Distribution of gas hydrates on the North Slope of Alaska (MORIDIS et al., 2004)

### 1.2 PRODUCTION OF METHANE FROM GAS HYDRATE RESERVOIRS

In conventional gas reservoirs, natural gas migrates to the recovery point via pressure gradients. For these reservoirs, the recovery rate is a function of the formation permeability and pressure gradients established between the reservoir and extraction well(s). Natural gas recovery

from hydrate-bearing deposits requires additional energy to dissociate the crystalline water lattice that forms the gas hydrate structure. A variety of methods have been proposed for producing natural gas from hydrate deposits: 1) thermal stimulation, where the temperature is increased above the hydrate stability region; 2) depressurization, where the pressure is decreased below the hydrate stability region; 3) chemical injection of inhibitors, where the temperature and pressure conditions for hydrate stability are shifted; and 4) CO<sub>2</sub> or mixed CO<sub>2</sub> and N<sub>2</sub> exchange, where CO<sub>2</sub> and N<sub>2</sub> replace CH<sub>4</sub> in the hydrate structure. Each of these methods is briefly reviewed in the sections that follow.

### **1.2.1 Thermal Stimulation**

Gas hydrate production via thermal stimulation recently has been investigated experimentally (TANG et al., 2005) and numerically (TSYPKIN, 2000; MORIDIS, 2003, 2004; MORIDIS et al., 2004; POOLADI-DARVISH, 2004). Technologies for implementing thermal stimulation include hot brine injection, steam injection, cyclic steam injection, fire flooding, and electromagnetic heating. Steam injection, cyclic steam injection and fire flooding suffer from high heat losses and the by-products of fire flooding can dilute the produced natural gas. Hot brine injection involves the injection of a saline aqueous solution at an elevated temperature into a gas hydrate bearing geologic reservoir. In general, brine injection yields a heating process that is dominated by advection of sensible heat carried by the brine. The dissolved salt lowers the gas hydrate dissociation temperature. Visual experiments of the dissociation process (TOHIDI et al., 2001) in glass micro-models indicate that during the dissociation process, the hydrate becomes colloidal and migrates advectively with the injected brine. Production experiments of Tang et al. (2005) indicate that the efficiency of the hot brine injection production methodology is dependent on the inlet brine temperature, injection rate, and initial hydrate saturation; where the measure of efficiency is the energy ratio, defined as the ratio of combustion heat of the produced gas over the heat input to the brine. Tang et al. (2005) concluded that lower temperatures and injection rates yield higher recovery energy ratios, as did higher initial hydrate saturations.

The downside of higher energy ratios realized through lower inlet temperatures and injection rates, however, are the lower production rates. Energy ratios for moderate to high temperatures and injection rates are on the order of 2.0, which means 50% of the recovered energy would be used to heat the injected brine. Another class of thermal stimulation technologies involves the injection of two fluids that react exothermally when mixed, such as the acidic- and basic-liquid approach proposed by Chatterji and Griffith (1998). The reaction of these two aqueous solutions would yield a hot salt solution.

### **1.2.2 Depressurization**

Gas hydrate production via depressurization is considered to be the most economically promising technology (COLLETT, 2004). The Messoyakha field in northern Russia is a natural gas accumulation, containing both free gas and hydrate-bearing formations, which has been produced by simple depressurization. The sustained production of natural gas from this field is due to the dissociation of gas hydrate into an underlying free-gas formation, and has demonstrated that gas hydrates are immediately producible using conventional methods. However, production rates are ultimately controlled by heat transfer toward the hydrate dissociation region. Gas production using depressurization at the Mallik site was numerically simulated (MORIDIS et al., 2004) as part of a study to analyze various production methods. A geothermal gradient of 0.03 °C/m across

the hydrate-bearing formation was assumed. The simulation results for a single vertical production well show temperatures dropping in response to depressurization of the formation and hydrate dissociation. The temperature decrease, however, is reversed as deeper warmer water is drawn to the well, providing the needed energy to sustain hydrate dissociation in the depressurized system. When augmented with either steam or hot methane ( $\text{CH}_4$ ) gas injection from a second well, natural gas production is superior in terms of the ratios of produced gas to water and fraction of produced hydrate  $\text{CH}_4$ .

Numerical depressurization studies for a one-dimensional radial confined reservoir with a central well were conducted using a linearization model (Ji et al., 2001). These studies and others (HONG and POOLADI-DARVISH, 2005; SUN et al., 2005) represent depressurization in its most basic configuration. As expected, simulation results indicate that hydrate dissociation rates and associated gas production rates are controlled by the far-field reservoir pressure and temperature, via energy supplied by natural gas advected from the far field to the dissociation front. Laboratory experimental studies of gas hydrate production via depressurization (LIU et al., 2002; SUNG et al., 2003) have been limited in number and scope. Because of the thermal self-regulation of gas hydrates, pure depressurization is a viable option for natural accumulations of gas hydrates, but may suffer from slow production rates. Sustained production using depressurization additionally requires a heat source. At the Messoyakha field, that energy source is likely heat transfer into the dissociation zone via thermal conduction and advection, which ultimately controls the production rate.

### 1.2.3 Inhibitor Injection

Thermodynamic inhibitors lower the hydrate formation temperature, which can result in hydrate dissociation when injected into a gas-hydrate-bearing formation (SUNG et al., 2002). The most common thermodynamic organic inhibitors are methanol, monoethylene glycol (MEG) and di-ethylene glycol (DEG) commonly referred to as glycol. Dissolved salts (e.g.,  $\text{NaCl}$ ,  $\text{CaCl}_2$ ,  $\text{KCl}$ ,  $\text{NaBr}$ ) can also be inhibitors. Whereas gas hydrate inhibitors are an effective methodology for preventing hydrate formation in engineering applications, their use in the production of natural gas hydrates is prohibitive from three perspectives: 1) environmental impact, 2) economic costs, and 3) thermal self regulation of gas hydrates.

### 1.2.4 Gas Exchange

Ohgaki et al. (1994; 1996) first advanced the concept of exchanging  $\text{CO}_2$  with  $\text{CH}_4$ , through experiments that showed  $\text{CO}_2$  to be preferentially clathrated over  $\text{CH}_4$  in the hydrate phase and demonstrated the possibility of producing  $\text{CH}_4$  gas by injecting  $\text{CO}_2$  gas. During the exchange process, Ohgaki et al. (1996) observed that the mole fraction of  $\text{CO}_2$  in the hydrate phase was greater than that in the gas phase. Seo et al. (2001; 2001) quantified this effect by noting that gas phase mole fractions of the hydrate formers (i.e.,  $\text{CH}_4$  and  $\text{CO}_2$ ) above 40%  $\text{CO}_2$  yielded hydrate phase mole fractions of  $\text{CO}_2$  in the hydrate phase greater than 90%. Pure  $\text{CH}_4$  and  $\text{CO}_2$  form structure I (sI) type hydrates (SLOAN, 1998) and their mixtures also form sI type hydrates (LEE et al., 2003). In forming mixed  $\text{CH}_4$  and  $\text{CO}_2$  hydrates, the  $\text{CH}_4$  molecules occupy both the large and small cages of type sI hydrates, whereas the  $\text{CO}_2$  molecules only occupy the large cages. Without hydrate dissociation, there is an upper limit to the substitution of  $\text{CO}_2$  for  $\text{CH}_4$  in hydrates. Lee et al. (2003) estimated that approximately 64% of the  $\text{CH}_4$  could be released via exchange with  $\text{CO}_2$ . In addition to equilibrium considerations, the heat of  $\text{CO}_2$  hydrate formation

(-57.9 kJ/mol) is greater than the heat of dissociation of CH<sub>4</sub> hydrate (54.5 kJ/mol), which is favorable for the natural exchange of CO<sub>2</sub> with CH<sub>4</sub> hydrate, because the exchange process is exothermic (SMITH et al., 2001). Although there are a considerable number of open literature publications on the CO<sub>2</sub>-CH<sub>4</sub> gas exchange concept, U.S. patent applications with very similar ideas have recently been filed.<sup>a,b</sup>

Neither Ohgaki et al. (1996) or Nakano et al. (1998) addressed the important issue of the kinetics of the gas exchange reaction. The first attempt to do so was performed by Uchida et al. (2001). Using a Raman spectroscopic method, they confirmed the swapping reaction at the hydrate-gas interface. Although the authors did not directly address the issue in their paper, their results suggested that the exchange mechanism was slow with induction times requiring several days. They did not address the more difficult question of the rate of CO<sub>2</sub> gas penetration further into bulk hydrate, beyond the first few hundred nanometers at the interface.

Multiphase exchange of CO<sub>2</sub> for CH<sub>4</sub> was proposed by Hirohama et al. (1996). Essentially, the method is identical to that proposed by Ohgaki et al. (1996) except extending to higher pressures such that CO<sub>2</sub> was in the liquid state instead of gaseous. The authors reported slow conversion kinetics with liquid CO<sub>2</sub> and in fact had much more rapid CH<sub>4</sub> recovery using gaseous N<sub>2</sub> instead. For liquid CO<sub>2</sub> injection, thermodynamic conditions can either favor CO<sub>2</sub> or CH<sub>4</sub> cage occupation. This transition occurs where the pure CO<sub>2</sub> and CH<sub>4</sub> temperature-versus-pressure equilibrium functions cross with increasing pressure above the gas-liquid CO<sub>2</sub> phase boundary.

Hydrate formation in geologic media that have a distribution of pore sizes will begin in the largest pore spaces and then continue into smaller pore spaces until the *in-situ* equilibrium condition is reached for a particular pore radius (CLENNELL et al., 1999). In addition to the equilibrium condition, porous media may affect other thermodynamic properties of hydrates. For example, in Goel's (2006) review of CH<sub>4</sub> production with CO<sub>2</sub> sequestration, a number of contrasting observations were revealed concerning the *in-situ* enthalpy of dissociation of CO<sub>2</sub> and CH<sub>4</sub> hydrates. Some research indicated that there was an increase in the heat of dissociation between *in-situ* and *ex-situ* conditions; whereas, other research indicated the opposite. Another example is the value of the lower quadruple point (ice-water-hydrate-gas) temperature and pressure for CH<sub>4</sub> and CO<sub>2</sub>, and the upper quadruple point (water-hydrate-gas-liquid CO<sub>2</sub>) for CO<sub>2</sub> hydrate between *in-situ* and *ex-situ* conditions; where, the *in-situ* conditions were determined for a porous media of limited pore-size distribution. In geologic media that have distribution of pore sizes, hydrates would form and dissociate over a range of temperatures and pressures according to the distribution of pore radii and accounting for the impact of salts in the residual pore water (MCGRAIL et al., 2007). The critical conclusion from Goel's (2006) review with respect to hy-

---

<sup>a</sup>Sivaraman, A. 2005. "Process to Sequester CO<sub>2</sub> in Natural Gas Hydrate Fields and Simultaneously Recover Methane." Gas Technology Institute, U.S. Patent Application No. 20050121200.

<sup>b</sup>Graue; A. 2006. "Production of Free Gas by Gas Hydrate Conversion." ConocoPhillips Company, U.S. Patent Application No. 20060060356.

drates in porous media is that to understand the gas exchange technology there is a need for quantitative estimates of formation and dissociation processes in geologic media core samples.

In the following section, we describe a set of laboratory experiments that were performed leading to a new approach for execution of the CO<sub>2</sub>-CH<sub>4</sub> exchange process in gas hydrate reservoirs that we call the Enhanced Gas Hydrate Recovery (EGHR) process.



## 2.0 EXPERIMENTAL

A series of laboratory experiments designed to investigate the feasibility of releasing CH<sub>4</sub> from natural gas hydrates by injecting a CO<sub>2</sub> rich fluid into a gas hydrate rich sediment is described below. Different forms of CO<sub>2</sub> (vapor, aqueous dissolved, and L<sub>CO2</sub>-L<sub>w</sub>) were tested and evaluated.

### 2.1 GAS PHASE EXCHANGE EXPERIMENTS

Although swapping CO<sub>2</sub>(g) for CH<sub>4</sub>(g) in bulk CH<sub>4</sub> hydrates is thermodynamically favorable, important factors such as kinetics of the reaction had not been fully investigated. Experiments were designed to measure the rate of CO<sub>2</sub> replacement in bulk CH<sub>4</sub> hydrate using a high pressure cell equipped with quartz viewing windows. Raman spectroscopy was used to monitor the CO<sub>2</sub>(g) penetration rate as a function of time at the solid-gas interface and into the bulk gas hydrate. No porous medium was used in these experiments.

Measurements for the rate of CO<sub>2</sub> replacement were determined by swapping out the head-space gas in a chilled, high-pressure cell containing bulk CH<sub>4</sub> hydrate and collecting Raman spectra at discrete time intervals and depth. Production of bulk CH<sub>4</sub> hydrate was achieved simply by pressurizing a measured amount of water in the Paar cell up to 1400 psig with methane and chilling in a freezer while a magnetic stir bar vigorously agitated the water. The identifying peak wavelengths for CO<sub>2</sub> hydrate were used to determine the mass transfer of CO<sub>2</sub>(g) into the bulk CH<sub>4</sub> hydrate. Depth of penetration verses time was determined by establishing peak intensity to baseline noise criteria.

A number of experiments were conducted at different temperatures under constant pressure (500 psig). An example of measured CO<sub>2</sub> penetration rates into bulk CH<sub>4</sub> hydrate at three different temperatures (0°, 2.5°, 4.5°C) is shown in Figure 2. As the temperature of the cell increases, the exchange rate of CO<sub>2</sub> for CH<sub>4</sub> in the bulk CH<sub>4</sub> hydrate increases. The maximum rate of penetration was 9 mm after 6 hours at 4.5°C. For this particular experiment, a duplicate run was conducted for 2.5°C and appeared to produce similar results (Figure 2). The calculated rate of CO<sub>2</sub> exchange is approximately 0.25 mm/h at 0°C. Increasing the temperature to 4.5°C increases the CO<sub>2</sub> rate of exchange to approximately 1.3 mm/h.

The gas exchange rate data show that penetration of CO<sub>2</sub> into bulk methane hydrate is a slow process and would be ineffective as a production method unless a means was employed to mix the CO<sub>2</sub> into the zone where the methane gas hydrates were present. Because of the low intrinsic permeability of gas hydrate bearing porous media, achieving such intimate mixing appears to be difficult without implementing some means to either stimulate the formation or induce bulk methane gas hydrate dissociation. As such, the

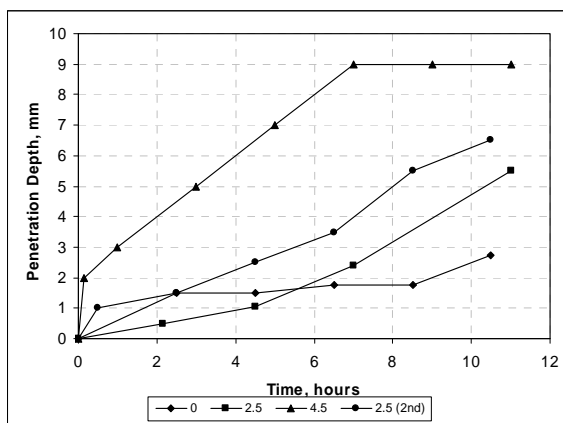


**Figure 2.** Carbon dioxide exchange in bulk CH<sub>4</sub> hydrate as function of time at three different temperatures (0°, 2.5°, and 4°C)

author's conclude that a strictly gas exchange method does not appear to be practical for gas hydrate production in the absence of other stimulation methods.

## 2.2 SINGLE-PHASE INJECTION EXPERIMENTS

The next set of experiments consisted of injecting a CO<sub>2</sub> rich fluid into a gas-hydrate bearing sand column. Extensive laboratory experimentation utilizing custom designed and fabricated equipment was used throughout this phase of the project.

All experiments were conducted in custom high-pressure columns constructed from a rigid polyurethane resin HYDEX® 301 (Dow Chemical Company). The five inch long, 37-ml volume columns consisted of one input port in the bottom and one outflow port in the top. Approximately 35g of 20/30 mesh Accusand (Unimin Corporation, Le Sueur, Minnesota) was used to fill the column before each experiment. A small piece of Spectra Mesh fluorocarbon filter was attached to the top inside area of the column to prevent sand from migrating out of the column. Pressurized water was supplied through ISCO syringe pumps. Column temperature was controlled by 3.05 m of 0.30 cm (outer diameter) copper tubing coiled around the cylinder portion of the column and connected to a Thermo Neslab (model RTE7) Digital One circulating water bath. For added temperature stability, a thermal blanket was placed on top and around the HYDEX® 301 column and copper tubing coil. Internal column temperature was monitored by two type T-thermocouples positioned in opposite ends of the column and connected to an Omega HH509R digital meter.

Gas volume measurements were conducted with a “J” tube type manometer assembly. After completion of the experiment, the HYDEX® 301 column was connected to a series of three calibrated tubes, with the last two tubes containing H<sub>2</sub>O. As the CO<sub>2</sub>-saturated H<sub>2</sub>O exited the HYDEX® 301 column, the H<sub>2</sub>O was trapped in the first tube (later weighed) and the evolved CO<sub>2</sub> gas displaced H<sub>2</sub>O from the second column into a third column. The displaced volume was used to calculate the amount of CO<sub>2</sub> present in the HYDEX® 301 column. The mass of water evolved during column depressurization was added to the residual mass of water in the column, which was determined by subtracting the known initial dry weight of the column.

Single-phase injections (CO<sub>2</sub>-saturated water) occurred in the experimental setup shown in Figure 3. At first, the Parr high-pressure reactor containing water was pressurized with CO<sub>2</sub> to 1040 psi, chilled to 15°C, and allowed to equilibrate over night. A line attaching the HYDEX® 301 column (sand packed) to a dip tube in the Parr reactor delivered CO<sub>2</sub> saturated water into the column.

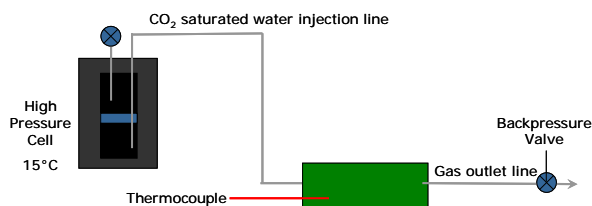


**Figure 3.** Schematic showing injection path of CO<sub>2</sub> saturated water into a sand packed HYDEX® 301 column

As shown in Figure 4, following the injection of CO<sub>2</sub>-saturated water, the column temperature steadily declines toward the water bath temperature of 2°C. Pressure on the column was maintained at 1040 psi. After 30 minutes, a significant thermal spike occurred, indicating the formation of CO<sub>2</sub> hydrate. This example, a temperature increase of 4°C above baseline, is typical of results obtained during these single-phase injection experiments.

For this particular experiment, the total amount of CO<sub>2</sub> and water in the HYDEX® 301 column was determined to be 0.53g and 6.8g respectively, giving a hydration number of 30. The ideal hydration number for sI gas hydrate is 5.75 mol-H<sub>2</sub>O per mol gas. However, complete filling of the gas hydrate cages is never achieved in practice and natural gas hydrates typically have hydration numbers of approximately 6 to 6.5. The very high measured ratio of 30 reflects the fact that CO<sub>2</sub>-saturated water contains insufficient total CO<sub>2</sub> to achieve complete conversion of the available water to gas hydrate. However, the experiment did prove the feasibility of injecting CO<sub>2</sub> rich fluid into a porous sand, dissociating the methane hydrate in the process. To obtain higher CO<sub>2</sub> hydrate saturations and thus improve process efficiency, a means to increase the amount of CO<sub>2</sub> available for conversion to gas hydrate is required. Our approach to achieving that objective is provided in the next section.

### 2.3 L<sub>CO2</sub>-L<sub>w</sub> EMULSION INJECTION EXPERIMENTS

Figure 5 shows the change in fluid density of CO<sub>2</sub> and water at 15°C as pressure increases. At sufficiently high pressure, CO<sub>2</sub> becomes a liquid and the density difference between water and liquid CO<sub>2</sub> is reduced to just a few percent. In contrast, the equilibrium pressure to form CO<sub>2</sub> hydrate at 15°C is approximately 43 MPa (6200 psia). Consequently mixtures of liquid CO<sub>2</sub> and water can be formed at 15°C to very high pressures and remain well outside the stability region where a CO<sub>2</sub> hydrate can form. Exploiting these unique physical properties of the CO<sub>2</sub>-H<sub>2</sub>O system is the fundamental idea behind our Enhanced Gas Hydrate Recovery method. Our concept is to utilize the small density contrast between liquid CO<sub>2</sub> and water to form a transiently stable microemulsion that could be injected into a porous medium containing gas hydrate. The emulsion can be formed with the proper ratio of CO<sub>2</sub> and water to ensure

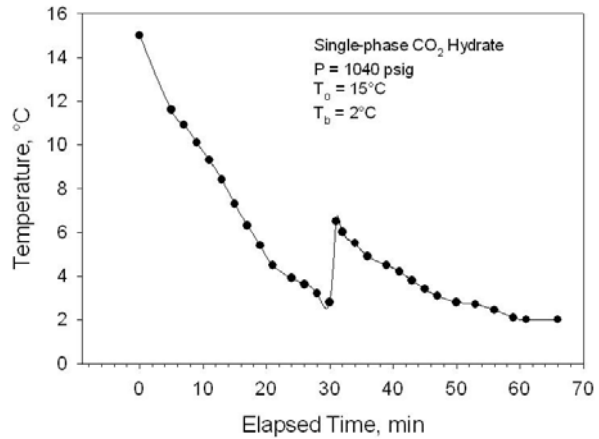


**Figure 4.** Temperature profile as a function of time after injection of CO<sub>2</sub> saturated water into a sand packed HYDEX® 301 column

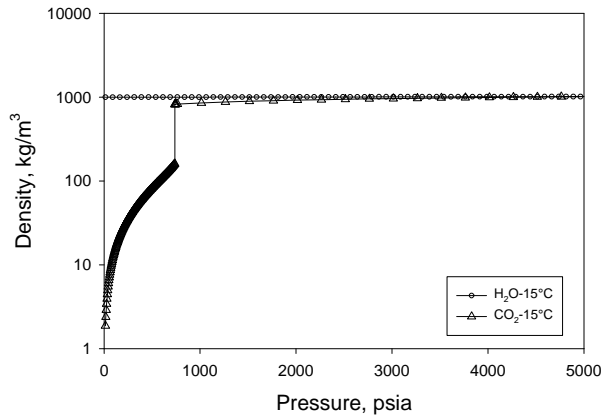


**Figure 5.** Density of liquid water and CO<sub>2</sub> as a function of pressure at 15°C

optimum conversion of the water to gas hydrate upon cooling into the stability region. The idea of injecting emulsions into porous media is not new; emulsions are used in a variety of subsurface applications including bioremediation, surfactant-enhanced remediation, and enhanced oil-recovery (YAN et al., 2006; CORTIS and GHEZZEHEI, 2007). However, we are unaware of any prior attempt to use high pressure liquid CO<sub>2</sub>-H<sub>2</sub>O emulsions to produce gas hydrates.

Our first attempt at injecting a two phase mixture of L<sub>CO2</sub> and L<sub>w</sub> was accomplished using the experimental setup shown in Figure 6. The high pressure Parr reactor containing 750 ml of deionized water was pressurized to 1000 psig with CO<sub>2</sub> and chilled to 15°C while being vigorously stirred. The HYDEX® 301 column packed with moist sand was pressurized with CH<sub>4</sub> to 1000 psig and chilled to -2.5°C, forming CH<sub>4</sub> hydrate rich sand. After overnight equilibration, the HYDEX® 301 column was connected to a 0.30 cm (outside diameter) stainless steel dip tube inserted into the Parr reactor with approximately 10.16 cm of tubing. The outflow (top) of the HYDEX® 301 column remained connected to an ISCO pump.

The L<sub>CO2</sub>-L<sub>w</sub> emulsion shown in Figure 7 was delivered to the inlet of the HYDEX® 301 column by extraction through the dip tube. Pressure on the HYDEX® 301 was maintained at 980 psig (ISCO pump), which was 20 psi lower than the Parr reactor. Upon opening the sampling valve on the Parr reactor, the L<sub>CO2</sub>-L<sub>w</sub> emulsion flowed at a maximum rate of 75 mL/min from the Parr reactor through the HYDEX® 301 column and through the back-pressure valve into an ISCO pump. Approximately 75 ml of emulsion was pumped through the sand before the outflow valve on the HYDEX® 301 column was closed. Pressure of 1000 psig was maintained on the HYDEX® 301 column by maintaining pressure in the Parr reactor with the ISCO pump.

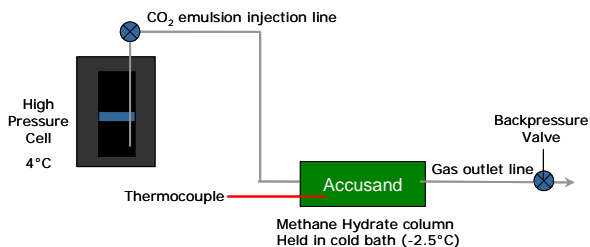


**Figure 6.** Schematic showing injection path of L<sub>CO2</sub>-L<sub>w</sub> into a CH<sub>4</sub> rich hydrate sand packed HYDEX® 301 column



**Figure 7.** View through quartz window into magnetically stirred pressure cell containing liquid CO<sub>2</sub> and water at 15°C and 1000 psig

Temperature changes occurring inside the HYDEX® 301 column after injection of emulsion were recorded for approximately four hours. Figure 8 shows the difference in temperature between the top and bottom of the HYDEX® 301 column over a period of 250 minutes. The cooling profiles show significant deviations from the expected parabolic cooling profile indicating hydrate formation within the column. The total amount of CO<sub>2</sub> and water in the sand was measured to be 2.72 g CO<sub>2</sub> and 6.80 g-H<sub>2</sub>O for a hydration number of 6.1. Hence, the injection method produced an almost ideal stoichiometric quantity of CO<sub>2</sub> and water for conversion to hydrate.

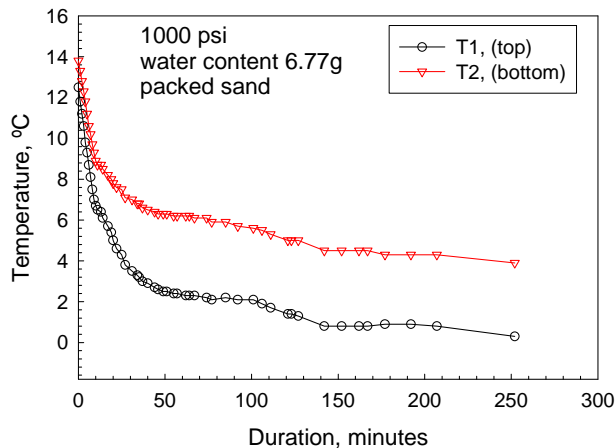


**Figure 8.** Temperature of sand packed column as a function of time, following injection of L<sub>CO<sub>2</sub></sub>-L<sub>w</sub> emulsion

We also performed an experiment injecting a three phase fluid containing L<sub>w</sub>-L<sub>CO<sub>2</sub></sub>-H. For this series experiment, the objective was to examine impacts of having preformed CO<sub>2</sub>-hydrate nuclei present in the injectate on the rate of CO<sub>2</sub>-hydrate formation post-injection. Consequently, CO<sub>2</sub>-hydrate was grown in the stirred Parr pressure vessel the day before injection and hydrate formation was confirmed using scanning laser Raman analysis. Utilizing the same experimental setup as described in Figure 6, a series of CO<sub>2</sub> hydrate injections was conducted.

Initially a known amount of distilled water was injected into the HYDEX® 301 column near the inlet thermocouple port to bring the volumetric water content in the cell such that 70% of the pore space was occupied with water. Weight measurements were recorded to accurately know the water content of the column. Methane gas was then injected into the column bringing the pressure of the cell up to 700 psig. The HYDEX® 301 column was then placed into a cooling bath held at room temperature and allowed to equilibrate for 2 hours. After this time, the cooling bath was set to -10°C and temperature recordings were made every 15 seconds. This temperature was maintained overnight to allow maximum equilibration for the methane-water/ice system. After a 20 hour time period elapsed, the cooling bath temperature was raised to -2.5°C and stabilized for 2 hours. Methane was then allowed to flow through the column and the resulting pressure differential was recorded. When gas flow between the outlets was induced, pressure drop across the column increased significantly because of the reduction in porosity upon hydrate formation. The system was allowed to flow until a constant pressure differential was maintained. After this process, flow was stopped and the column pressure was raised to roughly 600 psig.

Just prior to injection, the Parr reactor containing CO<sub>2</sub> hydrate was removed from the freezer and allowed to warm under ambient conditions. Mechanical stirring was started so as the solid hydrate mass broke up, CO<sub>2</sub> hydrate particulates formed that could enter the pore space. Once the aqueous phase was highly turbid with these nucleated CO<sub>2</sub>-hydrate particles (occurred at a temperature of 4°C), injection of a known amount of liquid was carried out through 0.63 cm tubing. The tubing connected the Parr reactor directly to the column containing methane hydrate. Water bath temperature where the column was immersed was maintained at -2.5°C. The volume

of tubing was also measured and used in the calculation for the total amount of injectant added to the column.

Shortly after injection of the turbid fluid, the column temperature in the cooling bath spiked to 8°C. This large heat gain could only occur from the heat released from formation of CO<sub>2</sub>-hydrate. Gas samples were also obtained from the outlet port of the column and analyzed by gas chromatography. Gas chromatography was used to analyze a sample taken 30 minutes after injection. Peak area analysis reveals no CO<sub>2</sub> vapor contained in the extracted gas phase, only methane. Hence, this experiment provides conclusive proof that multiphase CO<sub>2</sub> injection can be performed successfully in CH<sub>4</sub> hydrate bearing sediments, the free methane gas can be recovered, and the injected CO<sub>2</sub> retained as a gas hydrate in the sediment. However, we elected not to pursue this method further because the technique would be very difficult to implement in a field setting and injection of particulates was considered likely to lead to pore plugging.

## 2.4 CONTINUOUS MICROEMULSION INJECTION EXPERIMENTS

The injection experiments discussed in Section 2.3 were far from optimal in that use of pressure vessel inherently limits the volume of the two phase mixture that can be delivered and as is apparent from Figure 7, the droplet size of the liquid CO<sub>2</sub> spans a considerable range, much of which is far too large to pass through pore throats in typical sandy sediments. Consequently, a device was developed to supply a continuous stream of liquid CO<sub>2</sub> droplets suspended in water that is formed immediately before injection into a porous medium.

### 2.4.1 Microemulsion injector

Requirements for a microemulsion injector included combining liquid CO<sub>2</sub> and H<sub>2</sub>O to form an emulsion without using chemicals or additives. Multiple injector designs were tested. Initially the injector was placed up into the column, but sealing problems proved difficult to overcome. Mature designs positioned the injector inside the base of the pressure cells, eliminating o-rings and potential fluid leakage. The resulting product, shown in Figure 9, was fabricated from 304 stainless steel. The base measures 7.62 cm x 5.08 cm x 2.54 cm and has an inlet for CO<sub>2</sub>, H<sub>2</sub>O, and an outlet for the L<sub>CO<sub>2</sub>-L<sub>w</sub></sub> microemulsion. The bypass positioned on the side of the injector (Figure 9) is used to direct the emulsion away from the column, which is used in the initial stages of the injection experiments. Details on the internal configuration of the injector used to form micrometer size droplets of liquid CO<sub>2</sub> are not disclosed in this report due to intellectual property considerations.

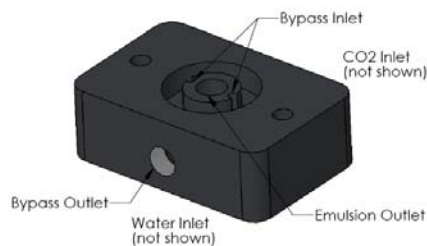


**Figure 9.** Schematic of microemulsion injector

Testing of the microemulsion injector was conducted through a number of experiments by changing the ratio of  $H_2O$  to  $CO_2$  as well as both the  $CO_2$  and  $H_2O$  injection rates. Each time, the microemulsion formed as expected. Figure 10 shows an example of the resulting microemulsion jets exiting the injector that were captured with high speed photography. The digital video images were captured by a Photron 1280 PCI high-speed digital camera equipped with a 105-mm lens. In all testing conducted, the camera was operated at 500 frame-per-second with a resolution of 1,280 by 1,024 pixels or at 1,000 frame-per-second with a resolution 1,280 by 512 pixels. The microemulsion is formed inside the injector before exiting the microemulsion outlet (Figure 10). At 500 fps, the individual discrete particles of  $CO_2$  were too small to distinguish. Additional images were collected at 1000 fps, which also showed no discernible detail of the emulsion structure. The large  $L_{CO_2}$  droplets apparent in Figure 10 result from droplet coalescence and collisions in the pressure cell long after exiting the injector.

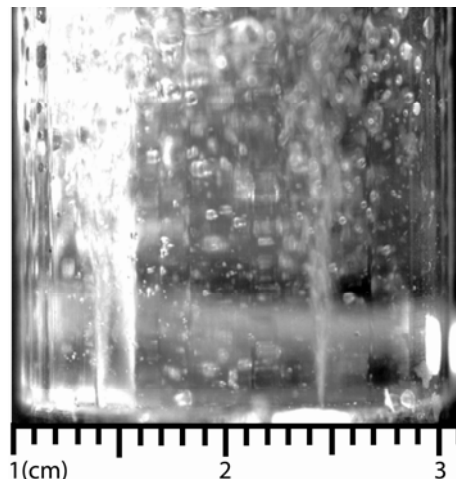


**Figure 10.** High speed photograph (500 fps) of  $L_{CO_2}$ - $L_w$  microemulsion created inside a sapphire high pressure column (2.54 cm OD).

#### 2.4.2 Microemulsion Injection Experiments

Originally,  $L_{CO_2}$ - $L_w$  microemulsion experiments were conducted in pressure cells constructed of HYDEX® 301, which had been commercially polished to appear transparent. Cell temperature was controlled by a Plexiglas shroud wrapped around the cell through which chilled fluid (antifreeze) was distributed by a bench top chiller. This experimental cell worked well for observing the formation of gas hydrates in porous sand. The material is robust and capable of withstanding multiple assemblies and unexpected pressure spikes without creating safety concerns. Additionally, the material is cost effective and has a long history of use as construction material for pressure cells. However, there were some disadvantages associated with using this type of resin. Characterization and confirmation of the formation of hydrates in a porous media were limited to thermal signatures, with no direct verification of the presence of gas hydrate via optical spectroscopic methods. The polished surface of the cell also reacted with  $CO_2$  and turned cloudy. Therefore, an alternate type of reactor material was required.

A thin walled high-pressure sapphire tube rated for 1300 psig was procured and integrated into the current cell design (Figure 11). The sapphire tube, measuring 15.24 cm long and 1.11 cm in diameter, allowed ex situ characterization by Raman spectroscopy of interstitial pore fluids and gas hydrates formed in porous media such as sand. As can be seen in Figure 12, the pressure cell is equipped with the microemulsion injector and a multi-channel thermocouple capable of monitoring internal cell temperature at six different locations. The cell temperature was controlled either by submersing in a water bath or by wrapping a coil of copper tubing around the cell and using chilled fluids as a heat transfer source. Preliminary experiments indicated problems with moisture condensation on the outside of the cell while collecting Raman spectra, which caused undesirable specular reflections. Also during these experiments, it was found that some startup time with the high pressure pumps was required before a consistent microemulsion could be generated for injection.

The base of the pressure cell was modified to include a small port for pre-injection fluids to bypass the column (Figure 12). At the start of the injection, H<sub>2</sub>O flow is required to reach a desired level before liquid CO<sub>2</sub> is introduced to create the emulsion. Directing this fluid out the bypass rather than through the porous media and out the top of the column is necessary to achieve optimal ratios of water and CO<sub>2</sub> in the column.

Once the desired flow for both H<sub>2</sub>O and liquid CO<sub>2</sub> are sufficient to generate the L<sub>CO<sub>2</sub></sub>-L<sub>w</sub> microemulsion, the bypass is closed and the emulsion is directed up through the CH<sub>4</sub> hydrate rich sand. Additionally, a vortex tube was incorporated into the cell design to control the cell temperature. This device uses ordinary compressed air to generate a stream of cooled air to -46°C. The stream of air is directed into a Plexiglas shroud surrounding the sapphire cell (Figure 12). This technique was very effective in cooling the column and eliminated interference with moisture condensation. Preliminary tests were conducted without sand in the column allowing for a visual confirmation that the injector produced a microemulsion at appropriate pressures and flow rates.

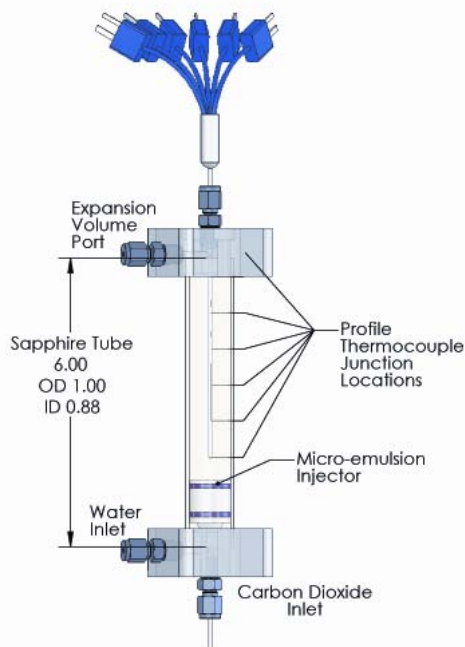


**Figure 11.** Schematic showing the high pressure sapphire cell equipped with a multi-port thermocouple probe

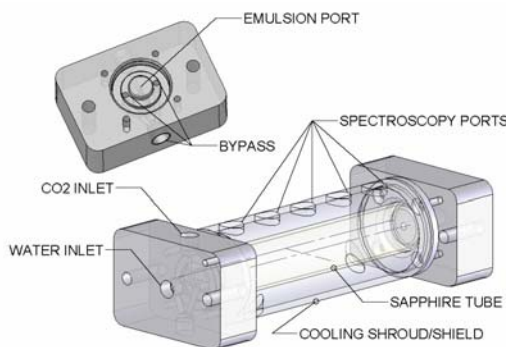


**Figure 12.** Schematic showing the redesigned high pressure sapphire cell equipped with a bypass port and cooling shroud

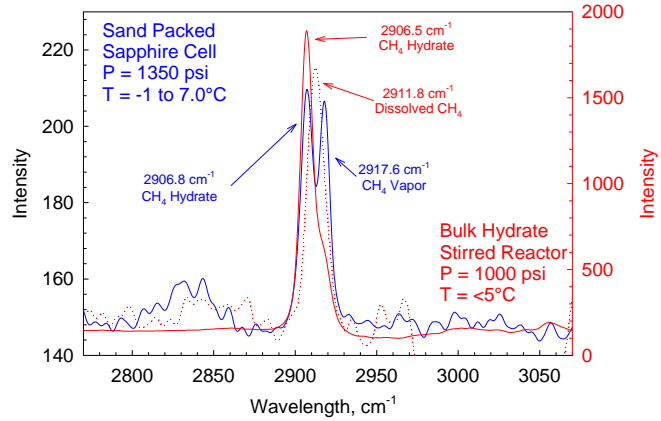
Methane hydrate rich sand was produced by packing the sapphire cell with 20/30 mesh Accusand, vacuum saturating with water to 80% pore volume, and then thermally cooling to 2°C. Following pressurization with CH<sub>4</sub> gas to 1300 psig, CH<sub>4</sub> hydrate formed spontaneously and the crystal formation could easily be observed visually. Generally, CH<sub>4</sub> gas hydrate initially appeared as a small white spot in the porous sand and then rapidly grew in all directions until complete coverage.

Figure 13 shows the Raman spectra taken of the white precipitate which produced a peak at 2906.8 cm<sup>-1</sup>, the main symmetrical band of CH<sub>4</sub> hydrate (SUM et al., 1997).

Also evident in Figure 13 is the shift in frequency between the vibrational band for free vapor CH<sub>4</sub> (2917.6 cm<sup>-1</sup>) and CH<sub>4</sub> hydrate (2906.8 cm<sup>-1</sup>). For reference, Raman spectra of bulk CH<sub>4</sub> hydrate, aqueous dissolved CH<sub>4</sub>, and CH<sub>4</sub> vapor as formed in a large mixing cell are provided in Figure 13.

Another important aspect of the experiment was to accurately identify the formation of CO<sub>2</sub> hydrate in sand. Accomplishing this task involved identifying each of the four phases of CO<sub>2</sub> (vapor, liquid, aqueous dissolved, and hydrate) by Raman spectroscopy in situ. Carbon dioxide vapor gives rise to Raman shifts at 1392.1 cm<sup>-1</sup> and 1288.6 cm<sup>-1</sup>. Examination of liquid CO<sub>2</sub> shows the Raman shifts at a slightly lower wavelength, 1390.0 and 1286.2 cm<sup>-1</sup>, respectively (Figure 14). As the CO<sub>2</sub> converts to gas hydrate, Raman peaks were observed at 1384.9 and 1281.1 cm<sup>-1</sup>, while for the dissolved CO<sub>2</sub>,

1387.3 and 1281.1 cm<sup>-1</sup>, respectively. As can be seen from Figure 14 the Raman shifts of the CO<sub>2</sub> molecule in the hydrate phase are very close to the CO<sub>2</sub> molecule in the dissolved phase, making the distinction of the two phases by Raman spectroscopy difficult (NAKANO et al., 1998).



**Figure 13.** Raman spectra of CH<sub>4</sub> as vapor, aqueous dissolved, and gas hydrate (porous media)

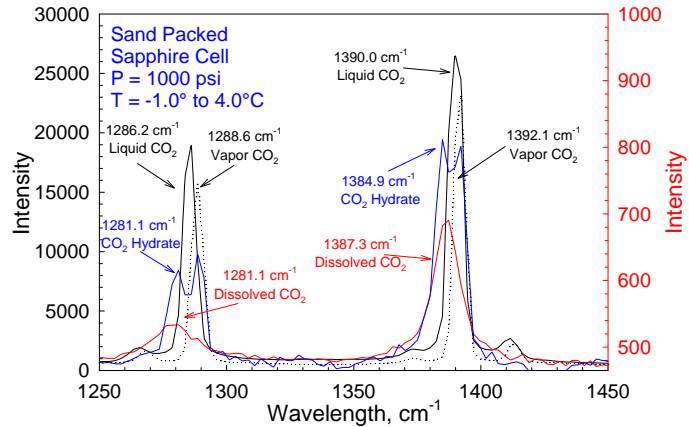


**Figure 14.** Raman spectra of CO<sub>2</sub> as vapor, liquid, aqueous dissolved, and gas hydrate (porous media)

Establishing identification parameters for each phase of CH<sub>4</sub> and CO<sub>2</sub> (gas, liquid, dissolved, and gas hydrate) by Raman spectroscopy allowed for the next phase of the injection experiment to start. After the formation of CH<sub>4</sub> hydrate, injection of the two phase L<sub>CO2</sub>-L<sub>w</sub> microemulsion fluid was initiated. A schematic diagram of the valving for the microemulsion experimental setup is shown in Figure 15. Both H<sub>2</sub>O and CO<sub>2</sub> are delivered by ISCO syringe pumps into the take up ISCO pump during the first segment of the injection. Bypassing the injector and packed sand column is critical while pressurizing the system with liquid CO<sub>2</sub> and H<sub>2</sub>O.

After achieving the desired flow rates and pressure, the separate fluids (H<sub>2</sub>O & liquid CO<sub>2</sub>) are diverted into the injector (Figure 15), located in the bottom of the cell, to form the L<sub>CO2</sub>-L<sub>w</sub> microemulsion. At first, the microemulsion is diverted out the side of the column, allowing time for the system to stabilize (Figure 15). After the L<sub>CO2</sub>-L<sub>w</sub> microemulsion is created, usually less than 15 seconds, the bypass valve is closed, diverting the microemulsion upwards through the sand packed column. As the relatively warm microemulsion fluid front (21°C) penetrates and moves through the porous CH<sub>4</sub> hydrate rich sand column being held initially at 2°C, CH<sub>4</sub> hydrate is seen to “dissociate” leaving behind pores filled with L<sub>CO2</sub>-L<sub>w</sub> microemulsion. During injection, the temperature of the column reaches 21°C and upon termination is allowed to return to the pre-injection temperature of 2°C. Cell pressure is maintained by the ISCO H<sub>2</sub>O pump. Conversion of CO<sub>2</sub> microemulsion into CO<sub>2</sub> hydrate was found to occur anywhere between 10 to 500 minutes, depending on the rate of cooling.

Experiments conducted in the HYDEX® 301 columns produced exothermic thermal signatures, an indication of hydrate formation, several degrees above the cell cooling profile. For example, Figure 16 shows an experiment conducted with moist sand packed into a HYDEX® 301 column. Following pressurization with CH<sub>4</sub> to 1000 psig and subsequent lowering of the temperature from 27°C to near 0°C, a significant temperature spike is observed after 18 minutes. The largest change in temperature occurs in the bottom third of the cell with a delta temperature

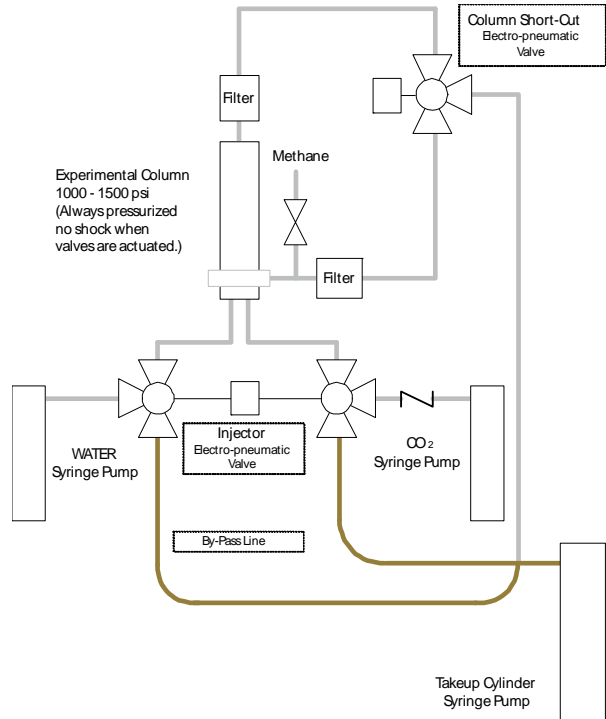


**Figure 15.** Microemulsion injection valving schematic

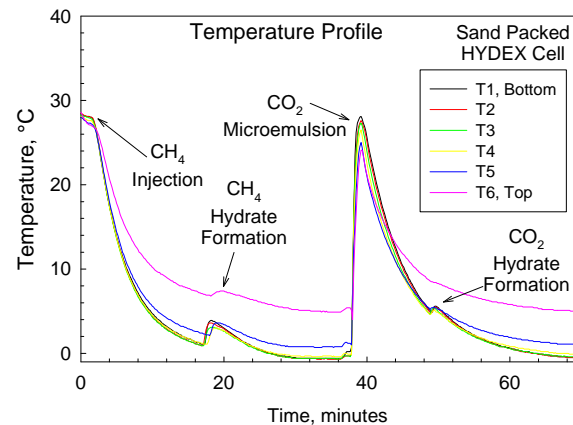


**Figure 16.** Temperature profile of HYDEX® 301 pressure cell during the formation of CH<sub>4</sub> hydrate, injection of CO<sub>2</sub> microemulsion, followed by the formation of CO<sub>2</sub> hydrate as a function of time

of over 1°C. The large temperature differential between the top of the cell (T6) and the bottom (T1) is directly related to the probe positioning. Thermocouple T6 is actually in the cap of the cell and is not embedded into the hydrated sand.

Growth of the hydrate was also evident from the white color change in the pore spaces and along the walls of the cell. Often, extra H<sub>2</sub>O from the moist sand collected near the bottom of the cell. Initial pressurization with CH<sub>4</sub> (through bottom of cell, Figure 15) caused free water to move upward and concentrate in an area resulting in reduced porosity. These areas typically contained dense CH<sub>4</sub> hydrate, but often caused problems in the second phase of the experiment, the L<sub>CO2</sub>-L<sub>w</sub> microemulsion injection. Precautions were taken to prevent excessive areas of water from forming during the CH<sub>4</sub> pressurization. A number of these experiments were conducted using different ratios of H<sub>2</sub>O and CO<sub>2</sub>, with the majority of tests being conducted with a ratio of 2:1. Fluid injection rates were typically kept at 40 and 20 ml/minute. Although the ISCO pumps are capable of delivering fluid at 200 ml/minute, the slower flow rates allowed more time to observe the warm fluid front move up through the column. Very similar results were observed in each experiment with the HYDEX® 301 columns.

Experiments conducted with a sapphire pressure cell followed the same injection process as described above. A typical thermal profile of an injection experiment is shown in Figure 17. As described earlier, similar exothermic signatures representing CH<sub>4</sub> hydrate and CO<sub>2</sub> hydrate formation within the sand packed column at distinct times were captured (Figure 17). For this experiment, the H<sub>2</sub>O and CO<sub>2</sub> volumetric ratio was maintained at 2:1. The maximum change in temperature (5°C) during CH<sub>4</sub> hydrate formation was measured in the upper portion of the cell 70 minutes after pressurization with CH<sub>4</sub> gas. Following the microemulsion injection, CO<sub>2</sub> hydrate began forming in the cell, which was visible as white pore filling material (Figure 17). Coinciding with formation of the pore filling white precipitate was a slight increase in cell temperature (0.3°C), confirmed by the measurements taken by the six port thermocouple. This exothermic event occurred 170 minutes in to the experiment, following the H<sub>2</sub>O-CO<sub>2</sub> microemulsion injection by 32 minutes.

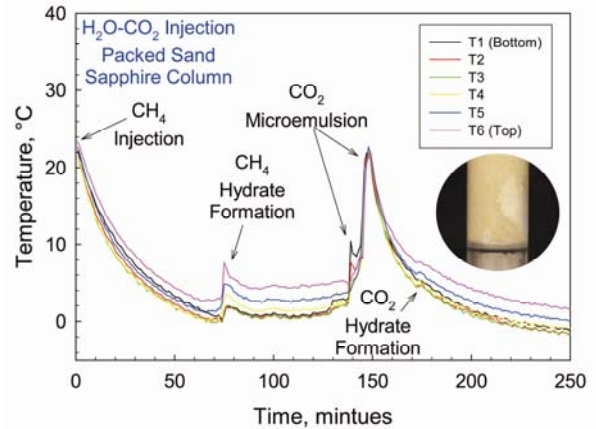


**Figure 17.** Temperature profile of sapphire high pressure cell during the formation of CH<sub>4</sub> hydrate, injection of L<sub>CO2</sub>-L<sub>w</sub> microemulsion, followed by the formation of CO<sub>2</sub> hydrate as a function of time

Five small diameter sampling tubes with valves were placed between the pressure cell and backup pump (Figure 15), allowing for the collection of discrete gas samples. A series of gas samples were collected during various stages of H<sub>2</sub>O-CO<sub>2</sub> microemulsion experiments, usually lasting 30 to 45 seconds. Each sample was subsequently analyzed on a residual gas analyzer (RGA). Monitoring masses 16 amu (CH<sub>4</sub>) and 44 amu (CO<sub>2</sub>) provided evidence of breakthrough of the injected CO<sub>2</sub>. Shown in Figure 18 are a few results taken from the HYDEX® 301 column experiments. The ratio of CH<sub>4</sub> to CO<sub>2</sub> is shown as a function of sample collection, which was typically 5 seconds apart from start to finish. For example, during experimental run 1 (Figure 18), five samples were collected in less than 45 seconds. Breakthrough clearly occurs when approximately 1 pore volume of the emulsion had been injected. Some CH<sub>4</sub> was still detected in Run 1 after 1 pore volume of injection indicating that some methane hydrate was still dissociating in addition to gas mixing at the leading edge of the emulsion front as would be expected. However, Runs #2 and #3 show that most of the CH<sub>4</sub> has been recovered by the time more than 1 pore volume of fluid has passed through the cell, verifying the efficiency of the L<sub>CO2</sub>-L<sub>w</sub> microemulsion in removing CH<sub>4</sub> hydrate.

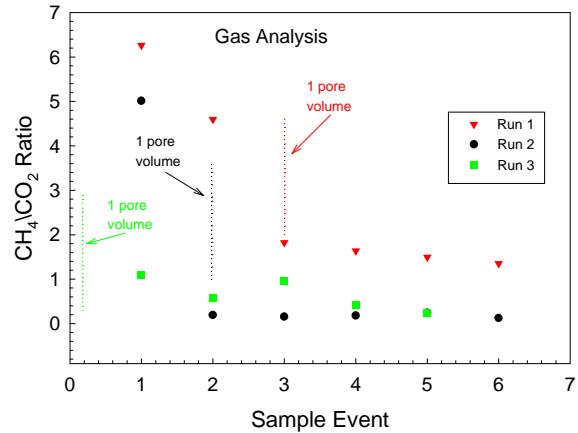


**Figure 18.** Gas analysis data collected during L<sub>CO2</sub>-L<sub>w</sub> microemulsion injection experiments

Post characterization of the CO<sub>2</sub> hydrated sand was conducted to evaluate pore space filling and condition of CO<sub>2</sub> hydrate. Determining if the L<sub>CO2</sub>-L<sub>w</sub> microemulsion remained stable in discrete particles and converted to CO<sub>2</sub> hydrate was essential to determine. Therefore, after completion of an injection experiment, a HYDEX® 301 column was chilled to -10°C and quickly depressurized to release any liquid CO<sub>2</sub> present in the column that had not converted to gas hydrate. The column was then submerged in liquid nitrogen and mechanically split to reveal the sand. Characterization of the sand aggregates was accomplished by optical light microscopy while samples were held partially immersed in LN<sub>2</sub>. An example of CO<sub>2</sub> hydrated sand is shown in Figure 19. No void areas where free liquid CO<sub>2</sub> would have existed were observed in the CO<sub>2</sub> hydrate rich sand. Figure 19 illustrates the complete filling of the porosity by CO<sub>2</sub> hydrate, suggesting complete saturation of the pores with the microemulsion fluid.



**Figure 19.** CO<sub>2</sub> hydrate rich sand extracted from a column injected with L<sub>CO2</sub>-L<sub>w</sub> microemulsion.

### 3.0 MODELING

The objective of the modeling work conducted in this investigation has been the development of a numerical simulation tool for analyzing the production of natural gas hydrates using conventional technologies, but also with the capabilities for considering the gas exchange technology. In the gas exchange production technology, clathrated methane is released when a more thermodynamically favorable molecule (e.g., carbon dioxide) replaces it in the hydrate. The outcome of this work has been a new operational mode for the STOMP simulator (WHITE and OOSTROM, 2006), which will be commonly referred to as STOMP-HYD. This operational mode of the simulator solves the governing conservation equations for heat, H<sub>2</sub>O mass, CH<sub>4</sub> mass, CO<sub>2</sub> mass, and NaCl (inhibitor mass) that describe the flow and transport of the conserved quantities through multifluid filled geologic media. The flow and transport equations are solved fully coupled, considering three mobile phases: 1) aqueous, 2) gas, and 3) liquid CO<sub>2</sub>; three immobile phases: 1) hydrate, 2) ice, and 3) precipitated salt, and the geologic media.

#### 3.1 MATHEMATICAL MODEL

The mathematical model for the STOMP-HYD simulator comprises governing conservation equations and associated constitutive equations that describe the flow and transport of heat and components through multiphase geologic media. In general the solved flow and transport equations are identical across the community of numerical simulators for methane hydrate production. STOMP-HYD, however, differs from hydrate production simulators in its use of capillary pressure functions to calculate phase saturations. This section describes the governing conservation equations and the calculation approach for the mobile and immobile phases.

##### 3.1.1 Governing Equations

The STOMP-HYD simulator solves five conservation equations, which can be expressed in two forms: 1) conservation of heat and 2) conservation of component mass (i.e., H<sub>2</sub>O, CH<sub>4</sub>, CO<sub>2</sub>, and NaCl). The conservation of heat equation, expressed in differential form, states that the time rate of change of internal energy equals the net transport of heat into the system, according to:

$$\frac{\partial}{\partial t} \left[ \sum_{\gamma=l,n,g,h,i,p} (\phi_D \rho_\gamma s_\gamma u_\gamma) + (1 - \phi_T) \rho_s s_s u_s + (\phi_T - \phi_D) \rho_l u_l \right] = \quad (1)$$

$$- \sum_{\gamma=l,n,g} \nabla (\rho_\gamma h_\gamma \mathbf{V}_\gamma) - \sum_{i=w,a,o} \nabla (h_g^i \mathbf{J}_g^i) + \nabla (\mathbf{k}_e \nabla T) + \sum_{\gamma=l,n,g} (h_\gamma \dot{m}_\gamma) + \dot{q}$$

where the phase flux is computed via Darcy's law according to:

$$\mathbf{V}_\gamma = - \frac{k_{r\gamma} \mathbf{k}}{\mu_\gamma} (\nabla P_\gamma + \rho_\gamma g \mathbf{z}_g) \quad (2)$$

and component diffusion is computed from molar gradients, considering molecular diffusion and hydraulic dispersion, according to:

$$\mathbf{J}_\gamma^i = -\phi_D \rho_\gamma s_\gamma \frac{M^i}{M_\gamma} (\tau_\gamma D_\gamma^i + \mathbf{D}_{h_\gamma}) \nabla \chi_\gamma^i. \quad (3)$$

Only the contribution of gas phase diffusion-dispersion is considered for the conservation of heat equation.

The conservation of component-mass equation, expressed in differential form, states that the time rate of change of component mass equals the net transport of component mass into the system, as given by:

$$\begin{aligned} \frac{\partial}{\partial t} \left[ \sum_{\gamma=l,n,g,h,i,p} (\phi_D \omega_\gamma^i \rho_\gamma s_\gamma u_\gamma) \right] = & - \sum_{\gamma=l,n,g} \nabla (\omega_\gamma^i \rho_\gamma \mathbf{V}_\gamma) \\ & - \sum_{\gamma=l,n,g} \nabla (\mathbf{J}_\gamma^i) + \sum_{\gamma=l,n,g} \omega_\gamma^i \dot{m}_\gamma \text{ for } i = w, a, o \end{aligned} \quad (4)$$

where, for mass transport, diffusion through all mobile phases is considered. Hydraulic dispersion is considered only for the transport of NaCl.

### 3.1.2 Phase Saturations

The conceptual pore-space model for the STOMP-HYD simulator includes five potential phases: aqueous, gas, liquid CO<sub>2</sub>, hydrate and ice. Hydrate and ice phases are assumed to be immobile and completely occluded by the aqueous phase. The mobile phases are assumed to decrease in wettability from aqueous to liquid CO<sub>2</sub> to gas phases. To reduce the number of phase conditions associated with the numerical solution, STOMP-HYD uses interfacial-tension-scale saturation versus capillary pressures to calculate phase saturations from the phase pressure primary unknowns. For conditions without liquid CO<sub>2</sub>, the aqueous saturation is calculated as a function of the scaled gas-aqueous capillary pressure, and for conditions with liquid CO<sub>2</sub>, the aqueous saturation is calculated as a function of the scaled liquid CO<sub>2</sub>-aqueous capillary pressure:

$$\bar{s}_l = \frac{s_l + s_h + s_i - s_{lr}}{1 - s_{lr}} = \text{func}(\beta_{gl} [P_g - P_l]) \text{ or } = \text{func}(\beta_{nl} [P_n - P_l]) \quad (5)$$

where, the scaling factors are computed as:

$$\beta_{gl} = \frac{\sigma^{ref}}{\sigma_{gl}}; \beta_{nl} = \frac{\sigma^{ref}}{\sigma_{nl} \cos(\theta_{nl})}; \beta_{gn} = \frac{\sigma^{ref}}{\sigma_{gn} \cos(\theta_{gn})}; \frac{1}{\beta_{gl}} = \frac{1}{\beta_{gn}} + \frac{1}{\beta_{nl}} \quad (6)$$

The functional forms shown in Equation (5) are generally those of van Genuchten (1980) or Brooks and Corey (1964). The closing Equation (6) provides continuity in the functions as liquid-CO<sub>2</sub> appears or disappears. The liquid-CO<sub>2</sub> saturation is computed indirectly from the total-liquid and aqueous saturations; where the total liquid saturation is computed as a function of the gas-liquid CO<sub>2</sub> capillary pressure:

$$s_n = s_t - (s_l + s_h + s_i); \bar{s}_t = \frac{s_l + s_h + s_i + s_n - s_{lr}}{1 - s_{lr}} = \text{func}(\beta_{gn} [P_g - P_n]) \quad (7)$$

For continuity in liquid-CO<sub>2</sub> transitions, the liquid-CO<sub>2</sub> pressure, as shown in Equation (8) is set to a critical pressure, whenever liquid-CO<sub>2</sub> is absent from the system:

$$P_n = \frac{\beta_{nl} P_l + \beta_{gn} P_g}{\beta_{nl} + \beta_{gn}}; \bar{s}_l = \frac{s_l - s_{lr}}{1 - s_{lr}}; \bar{s}_g = \frac{1 - \bar{s}_l}{1 - s_{lr}}; \bar{s}_n = \frac{s_n}{1 - s_{lr}} \quad (8)$$

The hydrate and ice saturations are computed indirectly from the hydrate-aqueous and the ice-aqueous capillary pressures, as shown in Equation (9), where ice saturation only occurs whenever the ice-aqueous interfacial saturation is less than the hydrate-aqueous interfacial saturation:

$$\begin{aligned} \bar{s}_h &= \bar{s}_l - \bar{s}_{hl}; \bar{s}_{hl} = \text{func}(\beta_{hl} [P_h - P_l]) \\ \bar{s}_i &= \bar{s}_l - \bar{s}_h - \bar{s}_{il}; \bar{s}_{il} = \text{func}(\beta_{il} [P_i - P_l]) \end{aligned} \quad (9)$$

The hydrate- and ice-aqueous capillary pressures are computed from the hydrate- and ice-aqueous interfacial tensions and radii of curvature, respectively:

$$P_h - P_l = \frac{2 \sigma_{hl}}{r_{hl}}; P_i - P_l = \frac{2 \sigma_{il}}{r_{il}} \quad (10)$$

where the hydrate-aqueous radius of curvature is computed from the difference in ex-situ hydrate equilibrium temperature and the system temperature, and the ice-aqueous radius of curvature is computed from the difference in freezing point temperature and system temperature (JIANG et al., 2001) given by:

$$r_{hl} = r_c \left[ 1 + \frac{(1 - \alpha)}{\log\left(\frac{T}{T_{eq}^{ex}}\right)} \right]; r_{il} = r_c \left[ 1 + \frac{(1 - \alpha)}{\log\left(\frac{T}{T_{fp}^{ex}}\right)} \right]; r_c = 3.6 \times 10^{-9} \text{ m}; \alpha = 1.66. \quad (11)$$

## 3.2 NUMERICAL SOLUTION

The governing conservation equations in the STOMP-HYD simulator are solved using integral volume differencing for spatial discretization on structured grids and a backward-Euler temporal discretization. These discretizations transform the governing equations to algebraic form; however, the resulting algebraic equations are nonlinear. Nonlinearities are resolved using multivariate Newton-Raphson iteration. This general numerical solution approach of spatial and temporal discretization and Newton-Raphson linearization is followed by the community of hydrate production simulators. STOMP-HYD differs in the selection of primary variable sets and the number of phase conditions. The use of capillary pressure functions to calculate hydrate and ice phase saturations greatly reduces the number of primary variable sets.

### 3.2.1 Discretization and Linearization

STOMP-HYD solves algebraic forms of the five governing conservation equations, Equations (1) through (5), that result from their discretization using the integral volume differencing technique on structured orthogonal grids, including boundary-fitted curvilinear grids. The backward-

Euler temporal discretization yields an implicit scheme, which requires the coupled solution of five nonlinear equations at each grid cell. Newton-Raphson iteration transforms the five nonlinear equations into a linear system of equations, but does not alter the requirement for a coupled solution of five unknowns at each grid cell (e.g., a problem involving 10K active grid cells requires a linear-system solve of order 50K). Partial derivatives required in the Jacobian matrix of the Newton-Raphson scheme are computed numerically, which greatly simplifies code development and also improves convergence performance during phase transitions. The linear-system solve yields corrections to the five primary variables, which are then used to calculate secondary variables and reconstruct the Jacobian matrix. For closure on the system of equations, all secondary variables must be calculated from the set of five primary variables.

### 3.2.2 Primary Variable Switching

As described above, STOMP-HYD solves for five unknowns or primary variables at each grid cell. One distinguishing feature of the simulator from others for methane hydrate production is that primary variable sets are principally phase pressure and vapor pressure as opposed to phase saturation and component mole fractions. By assuming that the aqueous phase never disappears the number of possible phase conditions (ignoring precipitated salt) is 16, where the saturation combinations are:

$$s_l = 1 \text{ or } s_l < 1; s_n = 0 \text{ or } s_n > 0; s_h = 0 \text{ or } s_h > 0; s_i = 0 \text{ or } s_i > 0 \quad (12)$$

With the hydrate and ice saturations defined through capillary pressure functions, the number of active phase conditions reduces to 4, where the saturation combinations are:

$$s_l = 1 \text{ or } s_l < 1; s_n = 0 \text{ or } s_n > 0 \quad (13)$$

The primary variable sets for the 4 active phase conditions can be further reduced to 2 by appropriately defining the gas and liquid CO<sub>2</sub> phase pressures, shown in Table 3.1.

**Table 3.1. Conceptual Phase Conditions and Primary Variable Sets**

Phase Condition	Energy	H <sub>2</sub> O Mass	CH <sub>4</sub> Mass	CO <sub>2</sub> Mass	NaCl Mass	$P_g, P_g^o$	$P_n, P_g^a$
$s_l = 1$ $s_n = 0$	$T$	$P_l$	$P_g^o$	$P_g^a$	$\zeta_l^s$	$P_g = P_l + \frac{\beta_{gl}}{\psi}$	$P_n = P_{nc}$
$s_l < 1$ $s_n = 0$	$T$	$P_l$	$P_g$	$P_g^a$	$\zeta_l^s$	$P_g^o = P_g - P_g^a - P_g^w$	$P_n = P_{nc}$
$s_l = 1$ $s_n > 0$	$T$	$P_l$	$P_g^o$	$P_n$	$\zeta_l^s$	$P_g = P_l + \frac{\beta_{gl}}{\psi}$	$P_g^a = P_{sat}^a$
$s_l < 1$ $s_n > 0$	$T$	$P_l$	$P_g^o$	$P_n$	$\zeta_l^s$	$P_g = P_g^a + P_g^o + P_g^w$	$P_g^a = P_{sat}^a$

The primary variable sets shown in Table 3.1 functionally allow for the solution of the governing equations for each phase condition. Application of the simulator to a variety of problems, however, has shown that the implementation of the primary variable set could be improved for cer-

tain phase transitions. Low liquid-CO<sub>2</sub> saturation conditions (i.e., less than 0.001) are difficult to resolve using the liquid-CO<sub>2</sub> pressure as the primary unknown. Including two additional phase conditions for low liquid-CO<sub>2</sub> saturations yields improved convergence and increased time steps. Low concentrations of CO<sub>2</sub> or CH<sub>4</sub> for unsaturated conditions are resolved more efficiently if the lower vapor partial pressure is used as the unknown, rather than using only the CO<sub>2</sub> vapor pressure. Therefore, the unsaturated phase condition without liquid CO<sub>2</sub> was split into two phase conditions. The resulting phase condition and primary variable set scheme, implemented into the code, is shown in Table 3.2.

**Table 3.2. Implemented Phase Conditions and Primary Variable Sets**

Phase Condition	Energy	H <sub>2</sub> O Mass	CH <sub>4</sub> Mass	CO <sub>2</sub> Mass	NaCl Mass	$P_g, P_g^a, P_g^o$	$P_n, P_g^a$
$s_l = 1$ $s_n = 0$	$T$	$P_l$	$P_g^o$	$P_g^a$	$\zeta_l^s$	$P_g = P_l + \frac{\beta_{gl}}{\psi}$	$P_n = P_{nc}$
$s_l < 1$ $s_n = 0$	$T$	$P_l$	$P_g^o$	$P_g$	$\zeta_l^s$	$P_g^a = P_g - P_g^o - P_g^w$	$P_n = P_{nc}$
$s_l < 1$ $s_n = 0$	$T$	$P_l$	$P_g$	$P_g^a$	$\zeta_l^s$	$P_g^o = P_g - P_g^a - P_g^w$	$P_n = P_{nc}$
$s_l = 1$ $s_n > 0$	$T$	$P_l$	$P_g^o$	$P_n$	$\zeta_l^s$	$P_g = P_l + \frac{\beta_{gl}}{\psi}$	$P_g^a = P_{sat}^a$
$s_l < 1$ $s_n > 0$	$T$	$P_l$	$P_g^o$	$P_n$	$\zeta_l^s$	$P_g = P_g^a + P_g^o + P_g^w$	$P_g^a = P_{sat}^a$
$s_l = 1$ $0 < s_n < 0.001$	$T$	$P_l$	$P_g^o$	$s_n$	$\zeta_l^s$	$P_g = P_l + \frac{\beta_{gl}}{\psi}$	$P_g^a = P_{sat}^a$
$s_l = 1$ $0 < s_n < 0.001$	$T$	$P_l$	$P_g^o$	$s_n$	$\zeta_l^s$	$P_g = P_g^a + P_g^o + P_g^w$	$P_g^a = P_{sat}^a$

### 3.3 APPLICATION

To demonstrate STOMP-HYD, the simulator has been applied to series of hydrate production scenarios involving idealized injection and extraction wells across a one-dimensional horizontal column of porous media. The horizontal domain is 20-m long, discretized into 20 grid cells with a cross-sectional area of 1 m<sup>2</sup>. Injection of liquid water with microemulsions of gaseous or liquid CO<sub>2</sub> occur at the left-hand boundary at a fixed pressure of 7 MPa, whereas, the right-hand boundary is maintained at 4.5 MPa and 3°C. The domain porous media is a 1-Darcy sandstone with an initial porosity of 0.3. Initially the domain is set to a pressure of 6 MPa, a temperature of 3°C and a CH<sub>4</sub>-hydrate saturation of 0.5. The complete list of hydrologic properties and initial conditions are shown in Table 3.1.

**Table 3.3. Hydrologic Parameters and Initial Conditions**

Parameter	Value
Porosity	0.3
Compressibility	$0.093 \times 10^{-5}$ 1/psi
Intrinsic Permeability	1 Darcy
Grain Thermal Conductivity	2.0 W/m K
Grain Specific Heat	700 J/kg K
Saturation-Capillary Pressure Model	van Genuchten (1980)
van Genuchten $\alpha$ Parameter	$0.132 \text{ m}^{-1}$
van Genuchten $n$ Parameter	2.823
Residual Aqueous Saturation	0.0
Gas-Aqueous Scaling Parameter	1.0
Liquid CO <sub>2</sub> -Aqueous Scaling Parameter	3.0
Gas-Liquid CO <sub>2</sub> Scaling Parameter	1.5
Hydrate-Aqueous Scaling Parameter	2.697
Ice-Aqueous Scaling Parameter	2.697
Aqueous Relative Permeability Model	Mualem (1976)
Gas Relative Permeability Model	Mualem (1976)
Liquid-CO <sub>2</sub> Relative Permeability Model	Mualem (1976)
Initial Pressure	6.0 MPa
Initial Temperature	3°C
Initial CH <sub>4</sub> Fraction of Hydrate Formers	1.0
Initial Hydrate Saturation	0.5
Initial Aqueous Saturation	0.5
Initial Dissolved Salt Concentration	$0.0 \text{ kg/m}^3$
Initial Dissolved CO <sub>2</sub> Concentration	$0.0 \text{ kg/m}^3$

A series of simulations was executed with STOMP-HYD that differed in the inlet boundary conditions. Microemulsions of liquid CO<sub>2</sub> and water were executed that varied in temperature and volumetric ratios, including pure water injections. Table 3.4 summarizes the suite of production scenarios.

**Table 3.4. Hydrate Production Scenarios**

Temperature	Microemulsion Volume Percent	Microemulsion State
15°C	0%	N/A
15°C	40%	Liquid CO <sub>2</sub>
15°C	50%	Liquid CO <sub>2</sub>
15°C	60%	Liquid CO <sub>2</sub>
20°C	50%	Liquid CO <sub>2</sub>
50°C	0%	N/A

### 3.3.1 Pure Water Injection

Two pure water injection simulations were executed at 15°C and 50°C. After injecting for 700 hr, the 15°C injectant produced 13.4% and the 50°C injectant produced 57.5% of the CH<sub>4</sub> mass through dissociation. To produce 75% of the CH<sub>4</sub> mass in the system through dissociation required 1254 hrs for the 15°C injectant, and 748.4 hrs for the 50°C injectant. As shown by the simulation results, CH<sub>4</sub> production rates for the pure water injectants are characteristically related to the inlet temperature, as the dissociation reaction is endothermic. Secondary hydrates form downstream from the dissociation front in both scenarios, with the 15°C injectant yield maximum secondary hydrate saturations of 0.55 and the 50°C injectant yield values of 0.61. Plots showing the hydrate saturations at points along the domain over time are shown in Figure 20 and Figure 21, respectively, for the 15 and 50°C injectant.

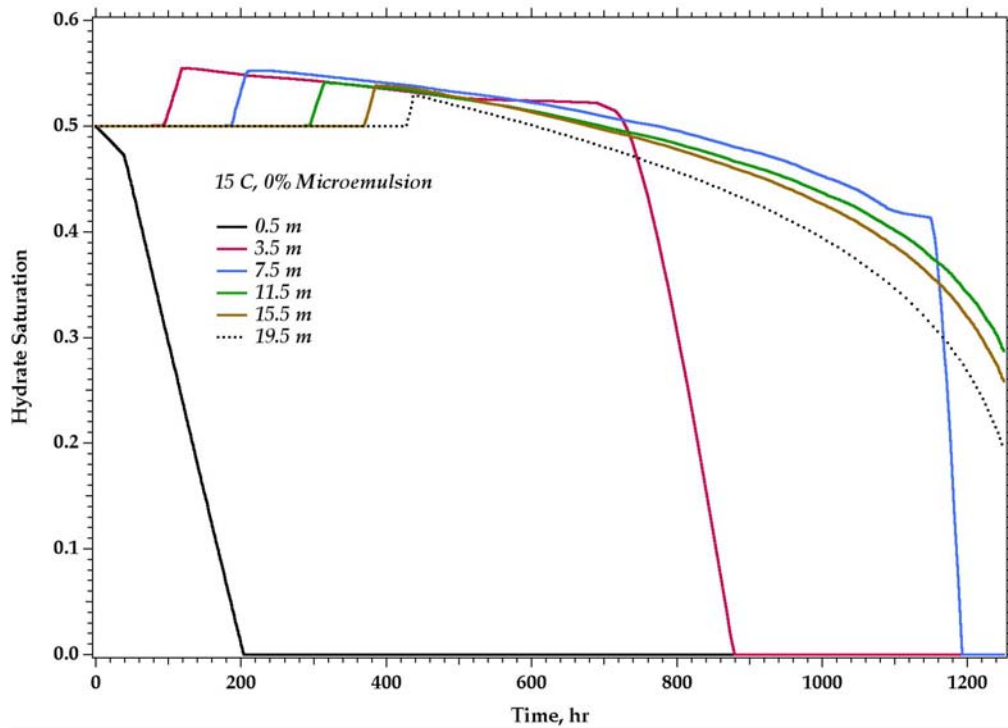


**Figure 20.** Hydrate saturation histories for 15°C pure-water injectant

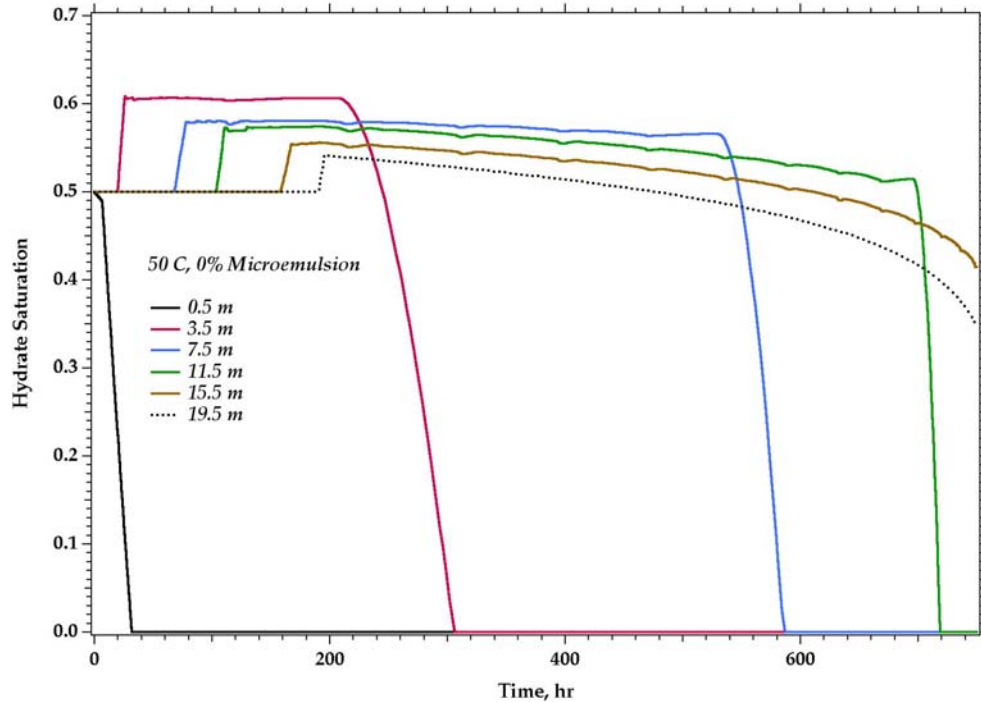


**Figure 21.** Hydrate saturation histories for 50°C pure-water injectant

### 3.3.2 Liquid-CO<sub>2</sub> Microemulsion Injectant

The saturation temperature for 7 MPa for CO<sub>2</sub> is 28.7°C, which means the CO<sub>2</sub> in microemulsion form will be in supersaturated liquid conditions for the 15 and 20°C injectant temperatures. The CH<sub>4</sub> hydrate production method for liquid CO<sub>2</sub> microemulsion involves principally exchange of CO<sub>2</sub> with CH<sub>4</sub> with some dissociation. Production continues until CO<sub>2</sub> breakthrough occurs at the domain outlet (i.e., producing well). Breakthrough was considered to have occurred when the mass fraction of CO<sub>2</sub> in the exiting gas phase reached 0.01. Breakthrough times, production percents at breakthrough, and maximum secondary hydrate saturations are shown in Table 3.5 for the liquid-CO<sub>2</sub> microemulsion injectant scenarios. Simulation results indicate that volumetric ratios of CO<sub>2</sub>/water have the greatest impact on breakthrough times, but generally no effect on production or maximum secondary hydrate saturations. Production times are considerably faster compared against the pure water injectant at 15°C, but production is limited by the breakthrough of CO<sub>2</sub> in the gas phase. Increasing the injectant temperature yields slightly faster breakthrough times and higher production. Plots showing the hydrate saturations at points along the domain over time are shown in Figure 22 and Figure 23, respectively, for the 15°C, 50% volume and 20°C, 50% volume liquid-CO<sub>2</sub> microemulsion injectant.

**Table 3.5. Liquid-CO<sub>2</sub> Microemulsion Injectant Simulation Results**

Injectant Conditions	Breakthrough Time	Production Percent at Breakthrough	Max. Secondary Hydrate Saturation
15°C, 40% Volume	272.1 hr	55.3%	0.72
15°C, 50% Volume	202.2 hr	55.5%	0.72
15°C, 60% Volume	149.2 hr	55.6%	0.72
20°C, 50% Volume	197.1 hr	56.0%	0.69

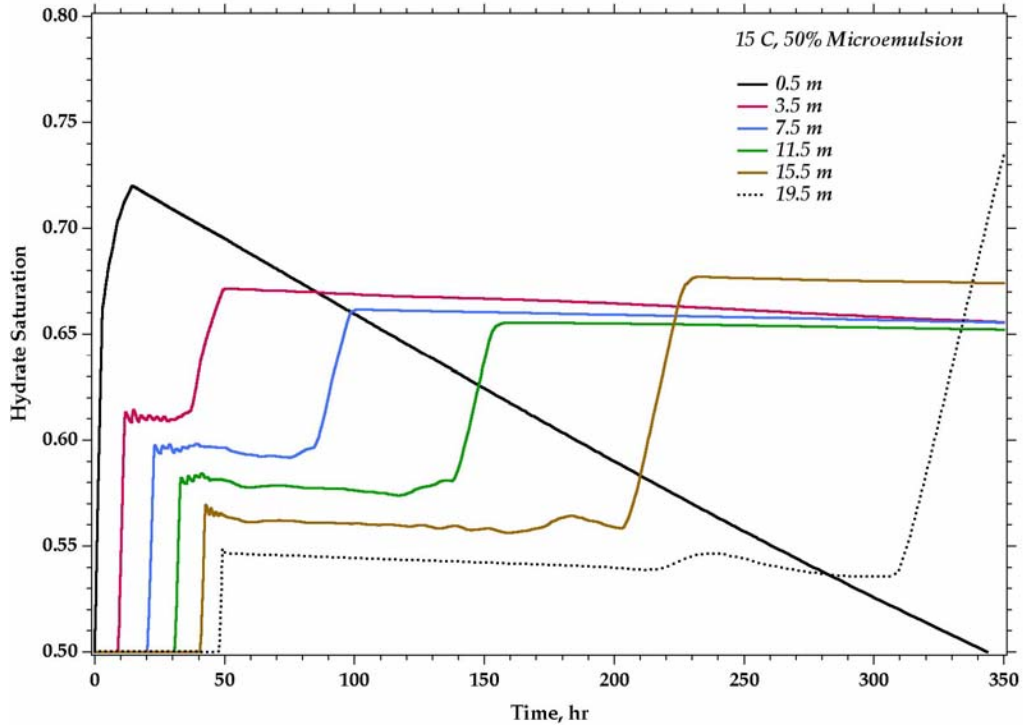


**Figure 22.** Hydrate saturation histories for 15°C, 50% volume liquid-CO<sub>2</sub> microemulsion injectant

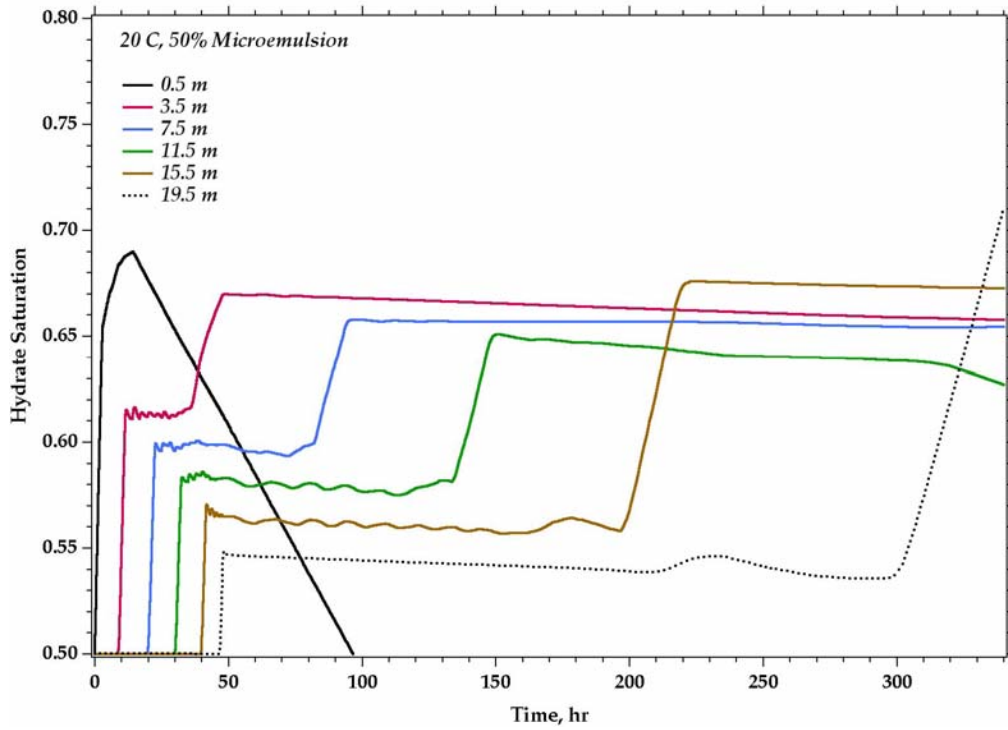


**Figure 23.** Hydrate saturation histories for 25°C, 50% volume liquid-CO<sub>2</sub> microemulsion injectant



## 4.0 DISCUSSION

The laboratory experiments presented in this report suggest that a strict gas exchange of  $\text{CO}_2$  for  $\text{CH}_4$  in bulk  $\text{CH}_4$  hydrate is too slow by several orders of magnitude to be considered an effective method of gas hydrate production. In contrast, both laboratory experiments and numerical modeling indicate that an EGHR process based on injecting a two phase emulsion of liquid  $\text{CO}_2$  and water at the proper volumetric ratio, can considerably enhance (3X and higher) production rate over injecting cool water ( $15^\circ\text{C}$ ) alone.

An important consideration in the EGHR technique is the range of reservoir conditions where the method might be applied. Figure 24 shows a compilation of well log temperature data reported by Collett (1993) for the Alaska North Slope. The vapor-liquid equilibrium line for  $\text{CO}_2$  is plotted on the same graph. The data suggest that the EGHR method could be implemented over a large fraction of the ANS, wherever deeper gas hydrate deposits exist. Typical ANS reservoir conditions would inject liquid  $\text{CO}_2$  with a density approximately 82% to 94% of the water phase. Note that  $\text{CO}_2$  hydrate would be stable under almost any conditions on the ANS short of very near the ground surface.

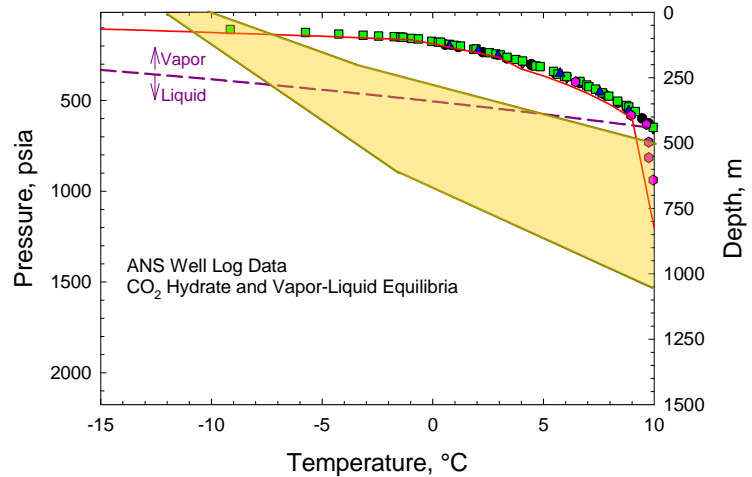


**Figure 24.** ANS well log temperature data shown as shaded area (after Collett 1993). Carbon dioxide hydrate and vapor-liquid equilibria are also plotted.

A number of other questions regarding application of the EGHR technique remain to be addressed. The bench scale experiments conducted in this project show no signs of coagulation into macrodroplets as the emulsion moves away from the injector. However, it remains to be investigated whether coagulation can be avoided at reservoir scale. Recent advances in modeling emulsion behavior in porous media (CORTIS and GHEZZEHEI, 2007) could help explore this issue. Additionally, an important restriction is that temperature of the water- $\text{CO}_2$  emulsion remains above the equilibrium point where  $\text{CO}_2$  hydrate could form in the wellbore or near-wellbore. Interruption of the supply of the emulsion fluid during production for an extended period could result in the premature formation of  $\text{CO}_2$  hydrate and plugging. Provisions for temporary introduction of heat may be needed to allow for flow interruptions, such as for well maintenance.

Although we have demonstrated a method for *continuous* production of a suitable  $\text{L}_{\text{CO}_2}\text{-L}_w$  emulsion, the device has only been tested at laboratory bench scale and is configured for injection into an essentially 1-D columnar domain. Development of a suitable downhole tool will be needed to supply the volumes of fluids required for a field trial. The injector tool design should be compatible with downhole conditions typical of gas hydrate formations. Wellbore completion requirements such as open hole, uncased, or perforated casing influence design parameters of the injector tool. Injection of the  $\text{L}_{\text{CO}_2}\text{-L}_w$  emulsion directly into the target formation is the most

important requirement. For example, the gas hydrate production research well, Mallik 5L-38, was cased and perforated at several different hydrate bearing zones (TAKAHASHI et al., 2005). Each zone was isolated with packers prior to testing. A similar approach could be used with a suitable downhole tool.

Redesigning the injector to deliver the microemulsion radially into the formation of interest is likely a priority. This might be accomplished by repositioning the emulsion outlets from the top of the injection tool to the sides as shown by the schematic in Figure 25. Surface warmed  $L_w$  and  $L_{CO_2}$  can then be directed into the injector from the high pressure lines. Use of produced water to form the emulsion would eliminate issues associated with disposal of these fluids in arctic conditions. Both rate and distance of formation penetration can be controlled from the surface by adjusting the  $L_{CO_2}$  and  $L_w$  pumps.

There are several parameters associated with injecting a  $L_{CO_2}$ - $L_w$  microemulsion into a porous hydrate rich formation that are still unknown. Placement of recovery wells including distance from the injection site, and spacing to maximize recovery of  $CH_4$  gas are a few of the important issues still unanswered. Identification and delivery logistics of an economical supply of  $CO_2$  are also essential factors in selecting an appropriate field site for demonstration. Additional numerical studies of the EGHR method are needed to address these questions and to guide design of an effective downhole tool.

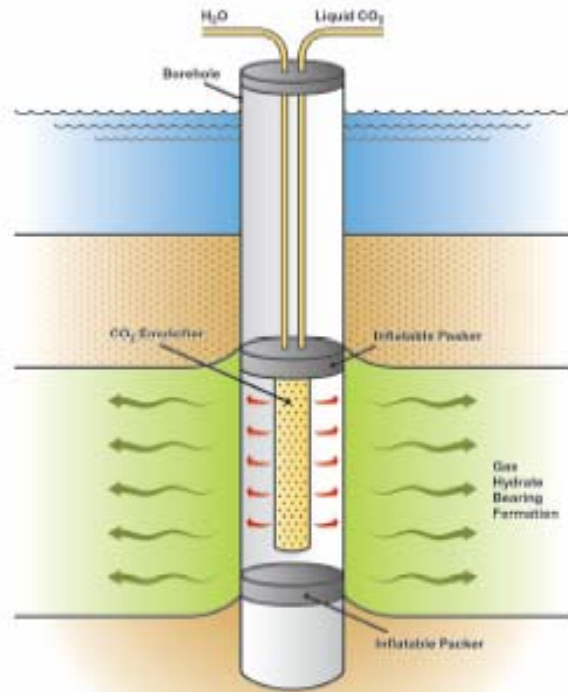


**Figure 25.** Schematic of down borehole injection tool

## 5.0 CONCLUSION

Through a proprietary method, a microemulsion injector was designed and tested to enhance production of methane hydrate-bearing porous media. A number of experiments were performed where a two-phase microemulsion ( $L_{CO_2}$ - $L_w$ ) was injected into a  $CH_4$  hydrate bearing sand packed column, a technique we call Enhanced Gas Hydrate Recovery (EGHR). The two-phase emulsion formed micrometer size droplets of liquid  $CO_2$  in the water phase at a ratio of approximately 44 g of  $CO_2$  per 103 g of water. This ratio was chosen to optimize filling of the small and large cages of the sI hydrate formed with  $CO_2$ . The temperature of the injectate was set significantly higher than the stability point of methane hydrate causing destruction of the gas hydrate crystalline lattice and release of enclathrated gas. The freed gas was displaced ahead of the microemulsion injection front and collected. After injection was stopped, the emulsion-containing sand was cooled into the stability region for  $CO_2$  hydrate. In every case,  $CO_2$  hydrate was observed to form visually, was monitored by an increase in temperature, and verified by Raman spectroscopy.

A numerical simulator, STOMP-HYD, was developed to investigate the feasibility of producing  $CH_4$  hydrate from geologic reservoirs beneath the permafrost and in deep ocean sediments. The simulator is capable of modeling  $CH_4$  hydrate production using the conventional technologies of thermal stimulation, depressurization and inhibitor injection, but additionally able to model the unconventional  $CO_2$  exchange approach. The principal objective in developing the simulator was to explore gas hydrate production using a combination of conventional and unconventional technologies using numerical simulation prior to testing the approaches in the field. Although the solved governing equations and constitutive equations are nearly identical to those of other methane hydrate production simulators, STOMP-HYD differs in use of capillary pressure functions to calculate hydrate and ice saturations. This approach considers the effect of porous media on the hydrate equilibrium function and ice freezing point (i.e., the hydrate and ice saturations are functions of the difference in system temperature and *ex-situ* hydrate equilibrium temperature and *ex-situ* ice freezing point). Simple 1-D simulations comparing injection of cool water ( $15^\circ C$ ) alone with injection of a microemulsion (also at  $15^\circ C$ ), showed much higher ( $>3X$ ) production of  $CH_4(g)$  using the EGHR technique.

The EGHR concept described in this report clearly has potential for use in converting a portion of natural gas hydrate reservoirs into a usable energy source. There are several advantages to the EGHR process, including: 1) Replacing  $CH_4$  with  $CO_2$  in gas hydrated sediment is thermodynamically favorable and heat generated from formation of  $CO_2$  hydrate is approximately 20% greater than heat consumed from the dissociation of  $CH_4$ , resulting in a low grade heat source to facilitate further dissociation of gas hydrate, 2) Once the  $CH_4$  is extracted and  $CO_2$  rich fluid fills pore space voids, the subsequent formation of  $CO_2$  hydrate would mechanically stabilize the formation eliminating subsidence concerns in some production situations, and 3) the process is carbon neutral in terms of replacing methane with  $CO_2$ , which is permanently sequestered in situ as a crystalline gas hydrate. Produced water could also be used to form the emulsion, eliminating a problematic disposal issue in arctic settings.



## 6.0 REFERENCES

- Brooks, R. H. and A. T. Corey. 1964. *Hydraulic Properties of Porous Media*. Hydrology Papers 3, Colorado State University, Fort Collins, Colorado.
- Chatterji, J. and J. E. Griffith. 1998. *Methods of Decomposing Gas Hydrates*. Patent No. 5,713,416, USA.
- Circone, S., S. H. Kirby, and L. A. Stern. 2005. "Thermal Regulation of Methane Hydrate Dissociation: Implications for Gas Production Models." *Energy Fuels* **19**(6):2357-2363.
- Clennell, M. B., M. Hovland, J. S. Booth, P. Henry, and W. J. Winters. 1999. "Formation of Natural Gas Hydrates in Marine Sediments 1. Conceptual Model of Gas Hydrate Growth Conditioned by Host Sediment Properties." *J. Geophys. Res.* **104**(B10):22985-23003.
- Collett, T. S., K. J. Bird, and L. B. Magoon. 1993. "Subsurface Temperatures and Geothermal Gradients on the North Slope of Alaska." *Cold Reg. Sci. Tech.* **21**(3):275-293.
- Collett, T. S. 2004. "Gas Hydrates as a Future Energy Resource." *Geotimes* **49**(11):24-27.
- Cortis, A. and T. A. Ghezzehei. 2007. "On the Transport of Emulsions in Porous Media." *J. Colloid Interface Sci.* **313**(1):1-4.
- Englezos, P. 1993. "Clathrate Hydrates." *Ind. Eng. Chem. Res.* **32**(7):1251-1274.
- Goel, N. 2006. "In Situ Methane Hydrate Dissociation with Carbon Dioxide Sequestration: Current Knowledge and Issues." *J. Pet. Sci. Eng.* **51**(3-4):169-184.
- Hirohama, S., Y. Shimoyama, A. Wakabayashi, S. Tatsuta, and N. Nishida. 1996. "Conversion of CH<sub>4</sub>-Hydrate to CO<sub>2</sub>-Hydrate in Liquid CO<sub>2</sub>." *J. Chem. Eng. Japan* **29**(6):1014-1020.
- Hong, H. and M. Pooladi-Darvish. 2005. "Simulation of Depressurization for Gas Production from Gas Hydrate Reservoirs." *J. Canadian Petrol. Tech.* **44**(11):39-46.
- Ji, C., G. Ahmadi, and D. H. Smith. 2001. "Natural Gas Production from Hydrate Decomposition by Depressurization." *Chem. Eng. Sci.* **56**(20):5801-5814.
- Jiang, Q., L. H. Liang, and M. Zhao. 2001. "Modelling of the Melting Temperature of Nano-Ice in Mcm-41 Pores." *J. Phys. Condens. Matter* **13**(20):L397-L401.
- Kvenvolden, K. A., G. D. Ginsburg, and V. A. Soloviev. 1993. "Worldwide Distribution of Subaquatic Gas Hydrates." *Geo-Marine Letters* **13**(1):32-40.
- Kvenvolden, K. A. 1995. "Natural-Gas Hydrate Occurrence and Issues." *Sea Tech.* **36**(9):69-74.

- Lee, H., Y. Seo, Y. T. Seo, I. L. Moudrakovski, and J. A. Ripmeester. 2003. "Recovering Methane from Solid Methane Hydrate with Carbon Dioxide." *Angewandte Chemie-International Edition* **42**(41):5048-5051.
- Liu, J., L. J. Yan, G. J. Cheng, and T. M. Guo. 2002. "Kinetics of Methane Hydrate Dissociation in Active Carbon." *Acta Chimica Sinica* **60**(8):1385-1389.
- McGrail, B. P., S. Ahmed, H. T. Schaefer, A. T. Owen, P. F. Martin, and T. Zhu. 2007. "Gas Hydrate Property Measurements in Porous Sediments with Resonant Ultrasound Spectroscopy." *J. Geophys. Res.* **112**(B05202), doi:10.1029/2005JB004084.
- Milkov, A. V., G. E. Claypool, Y. J. Lee, W. Y. Xu, G. R. Dickens, and W. S. Borowski. 2003. "In Situ Methane Concentrations, at Hydrate Ridge, Offshore Oregon: New Constraints on the Global Gas Hydrate Inventory from an Active Margin." *Geology* **31**(10):833-836.
- Moridis, G. J. 2003. "Numerical Studies of Gas Production from Methane Hydrates." *SPE Journal* **8**(4):359-370.
- Moridis, G. J., T. S. Collett, S. R. Dallimore, T. Satoh, S. Hancock, and B. Weatherill. 2004. "Numerical Studies of Gas Production from Several CH<sub>4</sub> Hydrate Zones at the Mallik Site, Mackenzie Delta, Canada." *J. Pet. Sci. Eng.* **43**(3-4):219-238.
- Moridis, G. J. 2004. "Numerical Studies of Gas Production from Class 2 and Class 3 Hydrate Accumulations at the Mallik Site, Mackenzie Delta, Canada." *SPE Reservoir Eval. Eng.* **7**(3):175-183.
- Mualem, Y. 1976. "A New Model for Predicting the Hydraulic Conductivity of Unsaturated Porous Media." *Water Resour. Res.* **12**:513-522.
- Nakano, S., K. Yamamoto, and K. Ohgaki. 1998. "Natural Gas Exploitation by Carbon Dioxide from Gas Hydrate Fields - High-Pressure Phase Equilibrium for an Ethane Hydrate System." *Proceedings of the Institution of Mechanical Engineers* **212**:159-163.
- Ohgaki, K., K. Takano, and M. Moritoki. 1994. "Exploitation of CH<sub>4</sub> Hydrates under the Nankai Trough in Combination with CO<sub>2</sub> Storage." *Kagaku Kogaku Ronbunshu* **20**:121-123.
- Ohgaki, K., K. Takano, H. Sangawa, T. Matsubara, and S. Nakano. 1996. "Methane Exploitation by Carbon Dioxide from Gas Hydrates - Phase Equilibria for CO<sub>2</sub>-CH<sub>4</sub> Mixed Hydrate System." *J. Chem. Eng. Japan* **29**(3):478-483.
- Pooladi-Darvish, M. 2004. "Gas Production from Hydrate Reservoirs and Its Modeling." *J. Petrol. Tech.* **56**(6):65-71.
- Seo, Y. T. and H. Lee. 2001. "Multiple-Phase Hydrate Equilibria of the Ternary Carbon Dioxide, Methane, and Water Mixtures." *J. Phys. Chem. B* **105**(41):10084-10090.
- Seo, Y. T., H. Lee, and J. H. Yoon. 2001. "Hydrate Phase Equilibria of the Carbon Dioxide, Methane, and Water System." *J. Chem. Eng. Data* **46**(2):381-384.

- Sloan, E. D., Jr. 1998. *Clathrate Hydrates of Natural Gases*. Marcel Dekker, Inc.
- Smith, D. H., K. Seshadri, and J. W. Wilder. 2001. "Assessing the Thermodynamic Feasibility of the Conversion of Methane Hydrate into Carbon Dioxide Hydrate in Porous Media." *First National Conference on Carbon Sequestration*, National Energy Technology Laboratory, Proceedings available at <http://www.netl.doe.gov/events/01conferences/carbseq/carbseq01.html>.
- Sum, A. K., R. C. Burruss, and E. D. Sloan. 1997. "Measurement of Clathrate Hydrates Via Raman Spectroscopy." *J. Phys. Chem. B* **101**(38):7371-7377.
- Sun, X., N. Nanchary, and K. K. Mohanty. 2005. "1-D Modeling of Hydrate Depressurization in Porous Media." *Transport in Porous Media* **58**(3):315-338.
- Sung, W. M., H. Lee, and C. Lee. 2002. "Numerical Study for Production Performances of a Methane Hydrate Reservoir Stimulated by Inhibitor Injection." *Energy Sources* **24**(6):499-512.
- Sung, W. M., H. Lee, S. Kim, and H. Kang. 2003. "Experimental Investigation of Production Behaviors of Methane Hydrate Saturated in Porous Rock." *Energy Sources* **25**(8):845-856.
- Takahashi, H., E. Fercho, and S. R. Dallimore. 2005. Drilling and Operations Overview of the Mallik 2002 Production Research Well Program. In *Scientific Results from Mallik 2002 Gas Hydrate Production Research Well Program, Mackenzie Delta, Northwest Territories, Canada*, Vol. Bulletin 585 (ed. S. R. Dallimore and T. S. Collett). Geological Survey of Canada, Vancouver, British Columbia.
- Tang, L. G., R. Xiao, C. Huang, Z. P. Feng, and S. S. Fan. 2005. "Experimental Investigation of Production Behavior of Gas Hydrate under Thermal Stimulation in Unconsolidated Sediment." *Energy Fuels* **19**(6):2402-2407.
- Tohidi, B., R. Anderson, M. B. Clennell, R. W. Burgass, and A. B. Biderkab. 2001. "Visual Observation of Gas-Hydrate Formation and Dissociation in Synthetic Porous Media by Means of Glass Micromodels." *Geology* **29**(9):867-870.
- Tsyppkin, G. G. 2000. Mathematical Models of Gas Hydrates Dissociation in Porous Media. In *Gas Hydrates: Challenges for the Future*, Vol. 912, pp. 428-436.
- Uchida, T., S. Takeya, T. Ebinuma, and H. Narita. 2001. Replacing Methane with CO<sub>2</sub> in Clathrate Hydrate: Observations Using Raman Spectroscopy. In *Proceedings of the Fifth International Conference on Greenhouse Gas Control Technologies* (ed. D. J. Williams, R. A. Durie, P. McMullan, C. A. J. Paulson, and A. Y. Smith), pp. 523-527. CSIRO Publishing, Collingwood, Australia.
- van Genuchten, M. T. 1980. "A Closed-Form Equation for Predicting the Hydraulic Conductivity of Unsaturated Soils." *Soil Sci. Soc. Am. J.* **44**:892-898.
- White, M. D. and M. Oostrom. 2006. *STOMP: Subsurface Transport over Multiple Phases, Version 4.0, User's Guide*. PNNL-15782, Pacific Northwest National Laboratory, Richland, Washington.

Yan, L., K. E. Thompson, and K. T. Valsaraj. 2006. "A Numerical Study on the Coalescence of Emulsion Droplets in a Constricted Capillary Tube." *J. Colloid Interface Sci.* **298**(2):832-844.

## Distribution

**No. of  
Copies**

**OFFSITE**

- 2 Robert Hunter  
ASRC Energy Services  
3900 C. Street, Suite 702  
Anchorage, AK 99503
- 2 Tao Zhu  
University of Alaska Fairbanks  
425 Duckering Building  
P.O. Box 755880  
Fairbanks, AK 99775-5880
- 1 Ray Boswell  
Strategic Center for Natural Gas & Oil  
U.S. Department of Energy  
National Energy Technology Laboratory  
3610 Collins Ferry Road  
P.O. Box 880  
Mail stop C02  
Morgantown, WV 26507-0880
- 1 E. Dendy Sloan, Jr.  
426 Alderson Hall  
Chemical Engineering Department  
Colorado School of Mines  
Golden, CO 804011
- 1 Timothy S. Collett  
US Geological Survey  
Denver Federal Center, MS-939  
Box 25046  
Denver, CO 80225 USA

- 1 Robert Vagnetti  
Strategic Center for Natural Gas & Oil  
U.S. Department of Energy  
National Energy Technology Laboratory  
3610 Collins Ferry Road  
P.O. Box 880  
Mail stop C02  
Morgantown, WV 26507-0880
- 1 Brent Sheets  
Arctic Energy Office  
U.S. Department of Energy  
P.O. Box 755910  
Fairbanks, AK 99775-5910

**No. of  
Copies**

**ONSITE**

- 6 **Pacific Northwest National Laboratory**
- |                |       |
|----------------|-------|
| B. P. McGrail  | K6-81 |
| H. T. Schaefer | K6-81 |
| M. D. White    | K6-81 |
| A. T. Owen     | K6-81 |
| P. L. Martin   | K6-81 |
| P. E. Long     | K9-33 |